Publications of the Astronomical Society of the Pacific, 137:104206 (26pp), 2025 October https://doi.org/10.1088/1538-3873/ae051e

Variability of Central Stars of Planetary Nebulae with the Zwicky Transient Facility. II. Long-timescale Variables including Wide Binary and Late Thermal Pulse Candidates*

Soumyadeep Bhattacharjee[1], Nicole Reindl[2], Howard E. Bond[3,4], Klaus Werner[5], Gregory R. Zeimann[6], David Jones[7,8], Kareem El-Badry[1], Nina Mackensen[2], Nicholas Chornay[9,10], S. R. Kulkarni[1], Ilaria Caiazzo[11], Jan van Roestel[12], Antonio C. Rodriguez[1], Thomas A. Prince[1], Ben Rusholme[13], Russ R. Laher[13], and Roger Smith[14]

[1] Department of Astronomy, California Institute of Technology, 1216 E. California Blvd, Pasadena, CA 91125, USA; sbhatta2@caltech.edu
[2] Landessternwarte Heidelberg, Zentrum für Astronomie, Ruprecht-Karls-Universität, Königstuhl 12, 69117 Heidelberg, Germany
[3] Department of Astronomy & Astrophysics, Penn State University, University Park, PA 16802, USA
[4] Space Telescope Science Institute, 3700 San Martin Dr., Baltimore, MD 21218, USA
[5] Institut für Astronomie und Astrophysik, Kepler Center for Astro and Particle Physics, Eberhard Karls Universität, Sand 1, 72076 Tübingen, Germany
[6] Hobby-Eberly Telescope, University of Texas at Austin, Austin, TX 78712, USA
[7] Instituto Astrofísico de Canarias, E-38205, La Laguna, Spain
[8] Departamento de Astrofísica, Universidad de la Laguna, E-38206 La Laguna, Tenerife, Spain
[9] Institute of Astronomy, University of Cambridge, Madingley Road, Cambridge CB3 0HA, UK
[10] Department of Astronomy, University of Geneva, Chemin d'Ecogia 16, 1290 Versoix, Switzerland
[11] Institute of Science and Technology Austria, Am Campus 1, 3400 Klosterneuburg, Austria
[12] Anton Pannekoek Institute for Astronomy, University of Amsterdam, 1090 GE Amsterdam, The Netherlands
[13] IPAC, California Institute of Technology, 1200 E. California Blvd, Pasadena, CA 91125, USA
[14] Caltech Optical Observatories, California Institute of Technology, Pasadena, CA 91125, USA
Received 2025 February 26; revised 2025 August 27; accepted 2025 September 8; published 2025 October 17

Abstract

In this second paper on our variability survey of central stars of planetary nebulae (CSPNe) using the Zwicky Transient Facility (ZTF), we report 11 long-timescale variables with variability timescales ranging from months to years. We also present preliminary analyses based on spectroscopic and/or photometric follow-up observations for six of them. Among them is NGC 6833, which shows a 980 days periodic variability with strange characteristics: "triangle-shaped" brightening in *r*, *i*, and WISE bands but almost coincidental shallow dips in the *g*-band. The most plausible explanation is a wide binary with the photometric period being the orbital period. Long-period near-sinusoidal variability was detected in two other systems, NGC 6905 and Kn 26, with periods of 700 days and 230 days, respectively, making them additional wide-binary candidates. The latter also shows a short period at 1.18 hr. We then present CTSS 2 and K 3-5, which show brightening and significant reddening over the whole ZTF baseline. A stellar model fit to the optical spectrum of CTSS 2 reveals it to be one of the youngest post-AGB CSPNe known. Both show high-density emission-line cores. We propose these to be late-thermal-pulse candidates, currently evolving towards the AGB phase. We then present recent HST/COS ultraviolet spectroscopy of the known wide-binary candidate LoTr 1, showing that the hot star is a spectroscopic twin of the extremely hot white dwarf in UCAC2 46706450. Similar to this object, LoTr 1 also has a fast rotating wide subgiant companion. We suggest that the long photometric period of 11 yr is the binary orbital period. Finally, we briefly discuss the ZTF light curves of the remaining variables, namely Tan 2, K 3-20, WHTZ 3, Kn J1857+3931, and IPHAS J1927+0814. With these examples, we present the effectiveness of the von Neumann statistics and Pearson Skew-based metric space in searching for long-timescale variables.

* Based in part on observations obtained with the Hobby-Eberly Telescope (HET), which is a joint project of the University of Texas at Austin, the Pennsylvania State University, Ludwig-Maximillians-Universität München, and Georg-August Universität Göttingen. The HET is named in honor of its principal benefactors, William P. Hobby and Robert E. Eberly.

Unified Astronomy Thesaurus concepts: Planetary nebulae (1249); Planetary nebulae nuclei (1250); Binary stars (154); Wide binary stars (1801); Post-asymptotic giant branch stars (2121); Light curves (918)

1. Introduction

Over the past decade, studies of photometric variability of central stars of planetary nebulae (CSPNe) have significantly improved our understanding of these systems. The majority of past works have been dedicated to the search for binarity in CSPNe in support of the common-envelope (CE) formation channel of planetary nebulae (PNe; see e.g.; Bond & Livio 1990; Balick & Frank 2002; De Marco 2009; Jones & Boffin 2017; Boffin & Jones 2019). Wide-field photometric surveys like the Optical Gravitational Lensing Experiment, Kepler-K2, Transiting Exoplanet Survey Satellite, and recently the Zwicky Transient Facility (ZTF) have together discovered more than a hundred binary CSPNe (Miszalski et al. 2009a, 2009b; Aller et al. 2020, 2024; Jacoby et al. 2021; Bhattacharjee et al. 2025; Chen et al. 2025). Periodicity has also led to the characterization of other phenomena like rotational variability caused by stellar spots (see for example Werner et al. 2019; Bond & Zeimann 2024), or pulsations of the hot CSPN (Bond & Meakes 1990; Ciardullo & Bond 1996; Hajduk et al. 2014; Córsico et al. 2021).

Though much less explored compared to periodic variables, CSPNe also exhibit aperiodic variability. One of the causes is strong winds in CSPNe, mostly causing "jittering" variability (see for example Handler et al. 1997; Arkhipova et al. 2012, 2013; Córsico et al. 2021). Unusual and large-amplitude aperiodic photometric variability of CSPNe has also led to the discoveries of R Coronae Borealis variables inside PNe, providing significant insights into the late thermal pulse formation channel of this class of stars (Asplund et al. 1997; Clayton & De Marco 1997; Gonzalez et al. 1998; Jeffery & Hambsch 2019; Rosenbush & Efimov 2015). Recently, transits of dust and debris disks was proposed as an explanation for the deep quasi-periodic dips seen in the nucleus of the planetary nebula WeSb 1 (Bhattacharjee et al. 2025; Budaj et al. 2025). These demonstrate the variety of causes that can induce photometric variability in CSPNe.

Most of the aforementioned phenomena occur on short timescales, ranging from a few minutes to a few days. On the other hand, there have only been very few instances of long-timescale photometric modulation in CSPNe. One example is PN IC 4997 (Aller & Liller 1966) which shows decade-long brightening and dimming periods, which may result from either a long-period binary (Kostyakova & Arkhipova 2009) or wind/mass loss variations (Arkhipova et al. 2020). Long-period light curve modulation due to binarity is seen in LoTr 5 (period of 7.4 yr, Kővári et al. 2019). Long-term photometric monitoring also resulted in the discovery of the ∼2600 days binary in pre-PN V510 Pup (Manick et al. 2021). Post-asymptotic giant branch (AGB) stars undergoing (very) late thermal pulses also show long-timescale photometric changes (van Genderen & Gautschy 1995 for FG Sge and Schaefer & Edwards 2015 for Stingray Nebula). There are a few other similar examples in the literature. However, there has not been any systematic search for long-timescale variability in CSPNe.

This is the second paper of the series conducting a systematic study of CSPN variability with ZTF (Graham et al. 2019; Masci et al. 2019). Here, we focus on the CSPNe showing long-timescale photometric variability in ZTF (the first one focused on the short-timescale variables, Bhattacharjee et al. 2025, hereafter Paper I). We find 11 objects showing prominent long-term variations in the light curve, making this by far the largest study of long-timescale variability in CSPNe. The rest of the paper is as follows. In Section 2, we briefly review the methodology employed in selecting the variable sources. In Section 3 we present our results. This includes spectroscopic observations of some of the objects and related analyses. Finally, we present our conclusions in Section 4.

2. Method and Sample Selection

The detailed procedure for the selection of variable CSPNe in ZTF data has been described in Paper I. We briefly review the methodology here. Our starting sample is the Gaia-EDR3-selected list of CSPNe presented in Chornay & Walton (2021). We restrict ourselves to sources with CSPN identification reliability >50%, resulting in 1812 CSPNe, of which ZTF data are recovered for 991 sources. Following this, we applied several photometric quality cuts, primarily to avoid sources where the extended nebula significantly affects the photometry. This reduced the number of sources to 490. To quantify variability, we calculate the Normalized Excess Variance metric (NEV) for the light curves. Using an appropriate cut on this metric value, we arrive at our final list of 94 highly variable CSPNe (HNEV sample). Among the HNEV sources, we classify 83 objects to be short-timescale variables (the focus of Paper I). The variability of the remaining 11 objects occurs on much longer timescales (months to years) and is well resolved with ZTF cadence. We classify these objects as long-timescale variables, which are the focus of this paper. The list of the 11 long-timescale variables is presented in Table 1. For convenience of readers, we also provide upfront the summary of our analyses in Table 2, the details being presented in the respective sections.

In Paper I, we had presented a two-dimensional metric space defined by the metrics von Neumann statistic (vonN) and Pearson Skew (SkewP) as a simple and novel technique to identify "exotic variables." Briefly, the former metric

Table 1
List of the Long-timescale Variable CSPNe

PNG	Name	R.A. (deg)	Decl. (deg)	Gaia DR3 ID	PNStat	PNRad (arcsec)	Rel	Known Period	ZTF Period
082.5+11.3	NGC 6833	297.4440	48.9611	2086764737566091136	T	0.3	1.0	⋯	∼980 days
061.4−09.5	NGC 6905	305.5958	20.1045	1816547660416810880	T	21.65	1.0	⋯	700 days?
084.6−07.9	Kn 26	320.7889	38.9700	1965268354805776896	T	55.0	1.0	⋯	230 days? 1.18 hr
044.1+05.8	CTSS 2	282.6953	12.6249	4504643171308707072	T	⋯	0.99	⋯	⋯
034.3+06.2	K 3-5	277.9409	4.0859	4283434037501295744	T	5.0	0.99	⋯	⋯
228.2−22.1	LoTr 1	88.7775	-22.9007	2917223705359238016	T	71.0	0.78	11.28 yr (1), 6.48 days (2)	6.48 days
069.6+15.7	Kn J1857.7+3931	284.4260	39.5167	2103243049609815296	P	75.0	1.0	⋯	⋯
032.5−03.2	K 3-20	285.5423	-1.8126	4262011019866089856	T	⋯	0.98	⋯	⋯
014.0−02.5	Tan 2	276.3213	-17.9413	4096278711670069248	T	3.0	0.83	⋯	⋯
045.0−12.4	WHTZ 3	299.4972	4.7921	4248349003725092608	T	46.0	0.99	⋯	⋯
044.3−04.1	IPHAS J192717.94 +081429.4	291.8248	8.2415	4296182638654046592	P	⋯	1.0	⋯	⋯

Notes. Description of the last five column names. PNStat: the PN status as reported in HASH. T and P stand for True and Probable, respectively. PNRad: radius of the PN as reported in HASH. Rel: CSPN assignment reliability fraction from Chornay & Walton (2021). Known Period: previously reported photometric period. ZTF Period: period(s) detected in ZTF light curve.
References– (1) Martínez et al. (2022) (2) Tyndall et al. (2013)

Table 2
Summary of Our Analyses for the Long-timescale Variables

Name	Summary
NGC 6833	"Triangle-shaped" periodic brightening in ZTF r, i and WISE bands associated with shallow dips in g. Eccentric binary with periastron interaction?
NGC 6905	Long periodic ($P \approx 700$ days, also $P \approx 245$ days?) near-sinusoidal variability. Wide binary?
Kn 26	Long periodic ($P \approx 630$ days, also $P \approx 230$ days?) near-sinusoidal variability: wide binary? Short period ($P \approx 1.18$ hr) arising from either pulsation or close binary.
CTSS 2	Steady brightening associated with significant reddening. Very young pre-white dwarf CSPN ($T_{\rm eff} \approx 90$ kK and $\log(g) = 4.5$). Late thermal pulse?
K 3-5	Very similar light curve behavior as CTSS 2, but no information about the CSPN. Late thermal pulse? Winds and dust?
LoTr 1	A very hot ($T_{\rm eff} \gtrsim 100$ kK) white dwarf with a rapidly rotating cool giant (9.7 $R_\odot$ and $T_{\rm eff} = 4590$ K) companion. Orbital period of 11 yr?
Kn J1857+3931	Long-timescale dimming over the whole ZTF baseline.
K 3-20	Long-timescale brightening (symmetric in appearance) associated with reddening. Part of a longer-periodic binary light curve?
Tan 2	Pointed dip in the beginning of ZTF light curve. Undergoing dip again after $\simeq 6.5$ yr. Wide-orbit debris eclipses or binary?
WHTZ 3	Short amplitude likely periodic long-term modulation in ZTF. Wide binary? Noisy data prevents detailed analyses.
IPHAS J1927+0814	Erratic high amplitude variability. Reason unclear: dust and debris? accretion?

quantifies the orderliness in the variability (against random variability from photon noise), and the latter differentiates between dimming and brightening events. We discussed that objects with low vonN ($\lesssim 1$) are often "interesting," i.e., objects which can teach us new phenomena. We demonstrated that the debris-disk candidate WeSb 1 lies in the low vonN space and its large negative SkewP successfully represents the deep eclipses. In Appendix A, we identify the long-timescale variables in this space and show its effectiveness in identifying them from large data sets. Such a discovery tool is expected to come in handy with upcoming large data sets with the advent of new surveys like the Legacy Survey of Space and Time (LSST; Ivezić et al. 2019).

3. Results and Analyses

Below we present the objects showing long-term photometric variability. We note up front that, except WHTZ 3, the ZTF variability of all the other objects below was recently reported in a completely independent work by (Chen et al. 2025, henceforth, C25). However, they provide no discussion on the origin of the variability or supplement their discovery with follow-up observations. In this work, we provide follow-

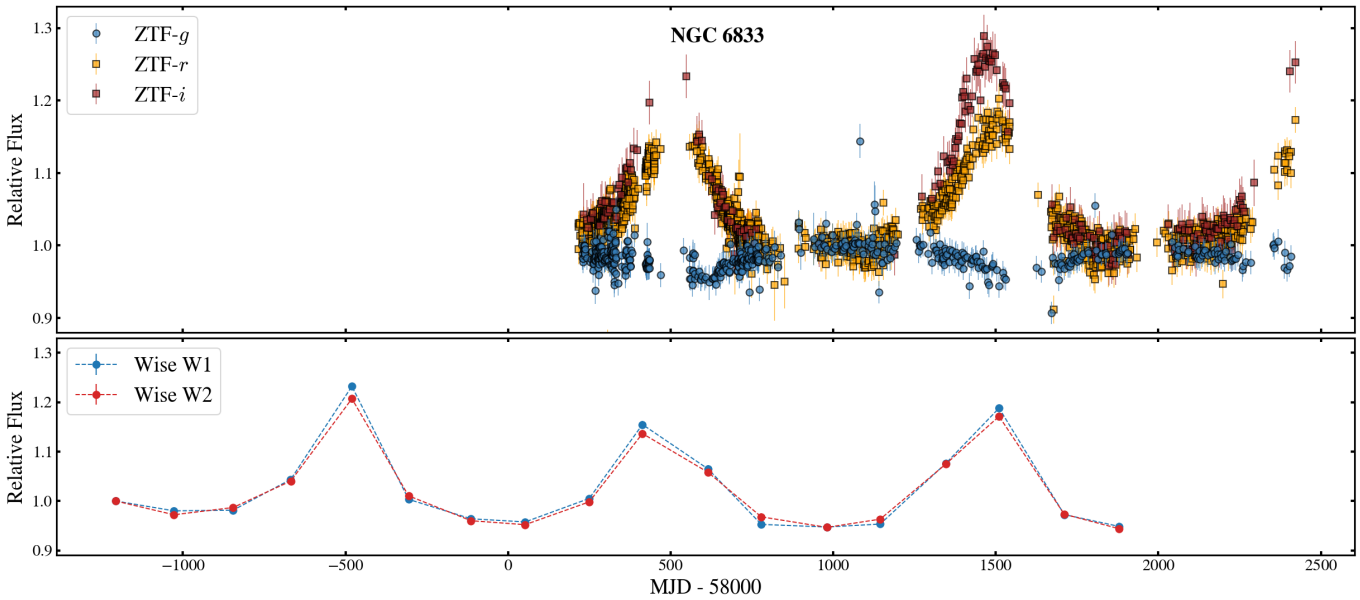

Figure 1. ZTF and neoWISE light curves for NGC 6833 (we do not show the two much older allWISE data points for ease of representation). The regular brightening events in ZTF-*r* and redder bands, coincident in the optical and mid-IR are evident. The shallow dip in the ZTF-*g* band corresponding to the peaks at the redder bands is also seen. For the details and discussion on this object, see Section 3.1.

up spectroscopic and photometric observations of six of the objects, shedding light on the nature of the objects and the origin of their variability. Additionally, we list the remaining five variables and urge further research by the community.

All the objects discussed here appear in the catalog of PN (candidates) detected by GALEX (Gómez-Muñoz et al. 2023). Five among these objects (LoTr 1, Kn J1857 +3931, NGC 6833, NGC 6905, and Kn 26) also appear in the catalog of hot subluminous stars by Culpan et al. (2022).

3.1. NGC 6833

NGC 6833 is a well-known PN and a "True PN" in the HASH catalog,[15] with an apparent diameter of 0.″6. Due to its compact angular size, current ground-based surveys cannot resolve the central star from the nebula. Thus, the recorded fluxes are a combination of both the star and the nebula. Images from the Hubble Space Telescope (see for example Hyung et al. 2010) reveal a box-like shape of the PN. NGC 6833 is present in various catalogs over decades, and has been the subject of several spectroscopic studies. Its photometric variability, however, remained unnoticed.

3.1.1. Light Curve and Spectroscopy

The ZTF light curve for NGC 6833 is shown in Figure 1 (top panel). Fortunately, this target has good *i*-band coverage. The most prominent feature is the regular brightening events in the ZTF *r* and the redder bands, with symmetric ingress and egress. The amplitude is in the range of 20%–30%, with the largest amplitude in *i*-band. We note here though that the nebular flux can reduce the perceived variability, so the intrinsic amplitude of the source (likely the central star) can be much higher (see a brief discussion in Section 3.1.2). The less prominent but more intriguing feature appears in the ZTF *g* band, which exhibits shallow (amplitude of $\lesssim$10%) dips nearly coincident with the peaks in the redder bands. The behavior is periodic and significant peaks appear in the Lomb-Scargle periodogram[16] in all the three ZTF bands. The result is shown in the top panel of Figure 2. The detected periods in the three bands are marginally different (which is not surprising with long periods), with a mean value of ∼980 days. The phase-folded ZTF light curve at this mean period is shown in the middle panel of the same figure. Here, the activity appears to be slightly phase-delayed from the redder to the bluer bands. However, the current data are insufficient to establish this property with high confidence.

We also present the WISE light curve in Figure 1. For better presentation, we only show the neoWISE light curve in this figure. The periodic brightening events are evident and coincident with the activity in ZTF. Unlike ZTF, the variability amplitude in both

[15] Hong Kong/Australian Astronomical Observatory/Strasbourg Observatory Hα Planetary Nebula (HASH, Parker et al. 2016) catalog is the largest catalog of PNe, serving as an important reference for Paper I and this work. It ranks its PN candidate entries as "True," "Likely," and "Probable" PNe, in decreasing order of their likeliness of actually being a PN. The True PNe are spectroscopically verified to be so.

[16] We first use the `astropy.timeseries` implementation of the Lomb-Scargle periodogram (Lomb 1976; Scargle 1982; VanderPlas 2018).

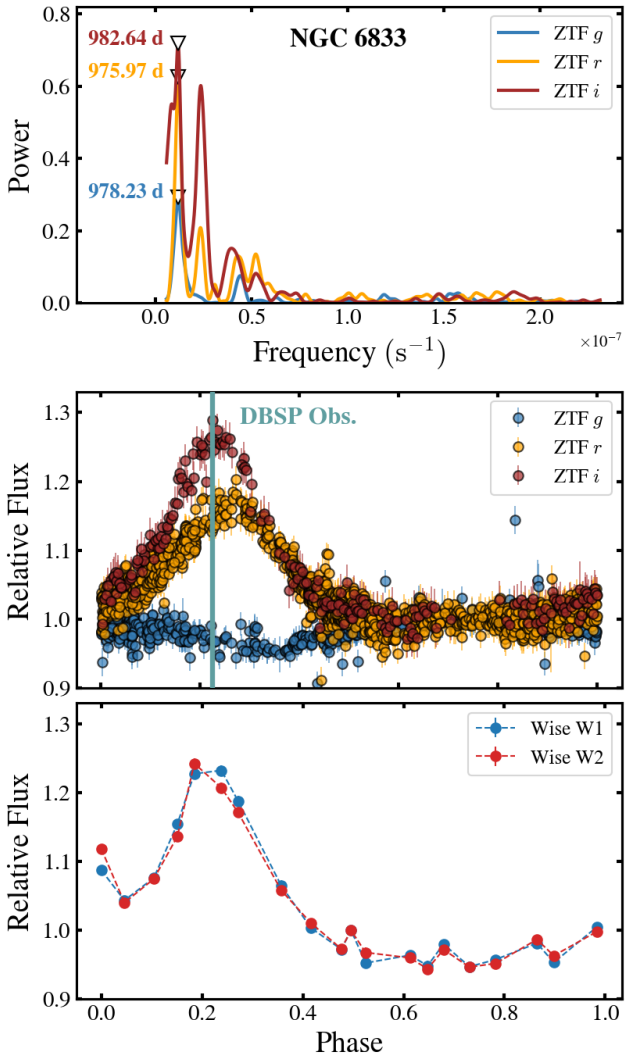

Figure 2. Top panel The Lomb-Scargle periodogram over for the ZTF light curve calculated over the period range of 50 days (2.3×10^{-7} Hz) to 2000 days (5.8×10^{-9}), with a resolution of 10^{-10} Hz. Significant peaks are detected at P ≈ 980 days. The power is strongest in the *i*-band, followed by *r*, and *g*. Middle panel ZTF light curve phase folded at the mean period of the three ZTF bands inferred from Lomb-Scargle of 978.95 days. The phase at the spectroscopic observation with DBSP has been marked. Bottom panel: WISE light curve (including the two allWISE data points) phase folded at the ZTF-inferred mean period. The first data points in each band are likely outliers.

W1 and W2 appears similar. The Lomb-Scargle periodogram applied to the WISE data shows a similar period of ≈980 days, as in ZTF. For consistency, we use the ZTF-inferred mean period to phase-fold the WISE data. The result is shown in the bottom panel of Figure 2. Except for the first data point (which happens to be the first allWISE reading and likely outlier affected by systematics relative to neoWISE), the phase-folded light curves closely resemble those of the red bands in ZTF.

Before any further discussion, we caution that the brightness of this object (≈12.3 mag in *g* and ≈12.8 mag in *r*) is very close to the saturation limit of ZTF (≈12–13 in all bands). In fact, in one of the ZTF fields, the reference image is indeed saturated in the *g*-band (where the object is brightest, mainly due to the very strong [O III] emission lines). Though such data points get rejected through the imposed quality cuts, the chance remains that the other flux readings are unreliable. To ascertain that this has not significantly affected the observed variability in the *g*-band, especially the dip, we checked the *g*-band light curve from the All Sky Automated Survey for SuperNovae (ASAS-SN) light curve provided at Sky Patrol V2.0[17] (Shappee et al. 2014; Hart et al. 2023), which has a larger saturation brightness (≈11–12 mag). The ASAS-SN *g*-band light curve displays similar behavior as ZTF and the dips are visible. The data quality, however, is worse than ZTF and thus not shown. For ZTF *r* and *i* bands, manual inspection shows that neither the reference nor the science images are saturated. We thus proceed with the assumption that the light curves are trustworthy.

At the time of this work, the object was at its photometric extremum. Assuming the ZTF period to be stable, the best estimate places the previous optical observations of Wright et al. (2005) and Hyung et al. (2010) at the quiescent phase. This prompted us to obtain another spectrum, with the DouBle SPectrograph (DBSP; Oke & Gunn 1982) attached to the Cassegrain focus of the Palomar 200-in Hale Telescope, to look for any significant changes. However, we could not find any notable difference between the spectra. The emission-line fluxes also agree well within error bars. The new spectrum is provided in Appendix B.

We use the spectrum to determine if the observed photometric variability can arise from solely the variation in the emission lines. We consider the ZTF-*i* band (≈7000–9000 Å) which shows the largest amplitude of ≈30%. We calculate the emission-line fluxes by subtracting the continuum. The emission line (including the Paschen series) contribution to the total flux is ≈25%. With this spectrum taken at the *i*-band maximum, this would require a significant decrement in the line strengths of all the emission lines to contribute meaningfully to the variability, which is unlikely. This leads us to conclude that there is a significant variation in the continuum. However, given the compact nature of the PN, it is not possible to separate the stellar and nebular continuum with the current data.

3.1.2. Discussion

The stable periodicity in the light curve strongly suggests binarity. The shape of the light curve with larger amplitude in redder bands[18] suggests an irradiation effect. This would mean that the photometric period is the binary orbital period. This would

[17] http://asas-sn.ifa.hawaii.edu/skypatrol/

[18] The strong emission lines, however, can significantly suppress any underlying continuum variability. To estimate the effect, we use the spectrum to subtract the emission lines and re-calculate the variability amplitudes in the ZTF bands. The amplitudes increased significantly. In fact, the ZTF *r* band now has a higher amplitude than the *i* band. This shows that the effect is significant and interpretation need to be made with sufficient care.

make it the fourth-longest known binary period inside a PN (after BD+33 2642 Van Winckel et al. 2014; Jones et al. 2017, LoTr 5, and NGC 1514 Jones et al. 2017). The large amplitude at such a long period suggests an eccentric binary. This is not a surprise as the other known long-period binaries are also eccentric. Irradiation, however, is not the only possible explanation. The light curves in the red bands resemble several RV Tauri systems showing long-term photometric modulation (known as the RVb phenomenon, see for example the light curves in Kiss & Bódi 2017). In this case, the widely accepted explanation to the variability is the phase-dependent dust-obscuration of the flux-dominant star in the presence of a thick circumbinary disc (Van Winckel et al. 1999; Gezer et al. 2015). In this case, too, the photometric period represents the orbital period.

Neither of the two scenarios above can individually explain the anti-correlated behavior in the g and the redder bands. A combination of both effects, however, could explain the variability. In an eccentric orbit, interaction (either directly between the stars or circumstellar disks) is enhanced near periastron. This can heat up the circumstellar dust leading to brightening in the red bands. Additionally, enhanced accretion can also lead to variability in emission lines, especially Hα. Such phenomena are sometimes observed during "pulsed accretion" processes in protostars (see for example Muzerolle et al. 2013, though the corresponding period is much shorter) and AGB binaries (Chen et al. 2017; Bollen et al. 2017). Irradiation of the companion by the hot CSPN can also contribute to the brightening in the red bands. The dip in the blue band can then be caused by the heavy dust obscuration of the white dwarf, which is the dominant contributor in this wavelength range. The stochastic nature of the interaction may also explain any offset between the blue and red extrema.

We now consider possible cases where the photometric period does not relate to binarity. Rotational modulation is unlikely as, in most cases, the light curves in different bands are in phase. C25 discusses α^2 Canum Venaticorum (ACV, a group of magnetic and chemically peculiar stars) a possibility as they also show anti-correlation between blue and red bands (see for example Gröbel et al. 2017; Faltová et al. 2021). However, the periods are much shorter (all known objects having $P \lesssim 10$ days, Faltová et al. 2021) compared to NGC 6833. We also consider the possibility of it being Be stars losing mass periodically due to pulsational instabilities. In most such cases however, the ingress time is significantly shorter than the egress time and the infrared amplitudes are much larger than observed in NGC 6833 (see, for example, the light curves presented in Froebrich et al. 2023). This makes this scenario, too, unlikely.

3.2. NGC 6905 and Kn 26

NGC 6905 is a spectroscopically well-studied PN. Its central star is a [WR]-type star with a temperature of ∼150 kK (Gómez-González et al. 2022). Spectral classifications of [WO] and [WC] have been given in the literature (e.g., Córsico et al. 2021 and Gómez-González et al. 2022). The star also shows pulsations with periods in the range of ∼700–900 s (Ciardullo & Bond 1996; Córsico et al. 2021). The nebula shows a bipolar morphology.

Kn 26, on the other hand, is a known quadrupolar PN (Guerrero et al. 2013), with Lanning 384 being its central star. Guerrero et al. (2013) finds the SED to be consistent with a blackbody of ∼70 kK. Unlike NGC 6905, Kn 26 has not been spectroscopically classified before. We obtained follow-up optical spectroscopy with the Large Binocular Telescope (LBT) which reveals it to have a weak emission-line type ([WELS]) nucleus (see Appendix C).

3.2.1. Light Curves

Both NGC 6905 and Kn 26 show long-term modulation in the ZTF light curve. The Lomb-Scargle periodogram over the long-period range (same as mentioned in caption of Figure 2) shows a very prominent peak at ≈700 days and a weaker peak at ≈245 days for NGC 6905. For Kn 26, two peaks of similar powers at ≈230 days and ≈630 days (the former being slightly dominant) appear in the periodogram. The flux semi-amplitude corresponding to the most prominent periods for the two objects are 2.6% ± 0.1% and 3.4% ± 0.2%, respectively.[19] The periods appear individually in the g and r bands (see Figures 3 and 4, top panel). It is interesting to note that the inferred periods in the two objects are quite similar. This, and the closeness of the periods to possible systematic timescales (seasonal breaks and yearly observation cycles) prompted several tests on the reality of the variability/periodicity. The details of the tests can be found in Appendix D. We find no reason to reject the periods.

In addition to the long periods, Kn 26 shows a short-period signal at 1.18 hr. When a Lomb-Scargle analysis over the short-period range (∼200 s to ∼100 days, same as used in Paper I) is applied on the raw ZTF light curve, the corresponding peak is visible, but it is subdominant to the 1 day cadence peak. However, the peak appears dominantly when the long-period modulation is subtracted out from the light curve and the periodogram is re-run. This result is presented in the third panel in Figure 4. The period is independently inferred in both the ZTF bands.

We used follow-up photometric observations to verify this period. Kn 26 was observed with the Wide Field Camera (WFC) at the Isaac Newton Telescope (INT) in 2021 July in the i-band with 120 s exposure, and in 2022 August in g- and

[19] C25 reports the 700 day period for NGC 6905 in their work. They, however, do not report these long periods in Kn 26. One might guess that this is due to the use of standard photometry against difference photometry. However, the long periods in both the objects are also recovered from the standard photometry data. This in turn shows that the photometric behavior is not an artifact of difference imaging.

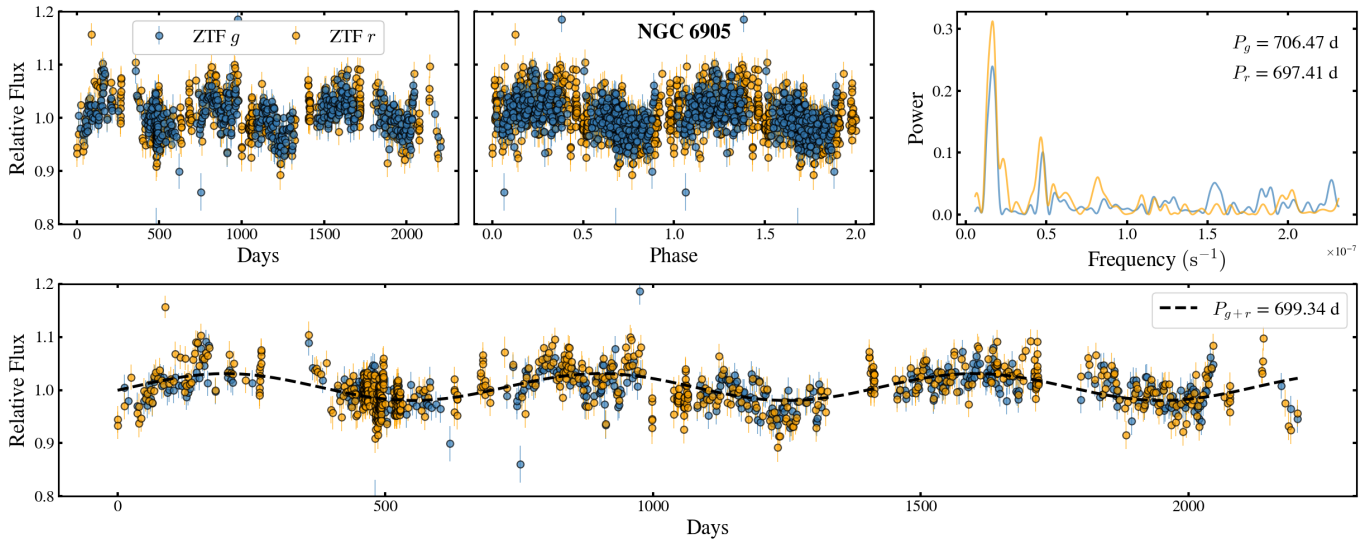

Figure 3. The long period variability in NGC 6905. Top Left: The raw ZTF light curve. Top Center: The ZTF light curve phased at the best period. Top Right: The periodogram for both the g and r bands. We also quote the respective periods in the panels. Bottom: Sinusoid at the best-fit period (in legend) of the combined $g + r$ data on the light curve for better visualization of the variability/periodicity.

r-bands with 90 s and 60 s exposures, respectively. The data were debiased and flat-fielded, before performing differential photometry of the central stars against non-variable field stars, all using standard astropy routines (Astropy Collaboration et al. 2018). Recently, we re-observed Kn 26 with the Caltech HIgh-speed Multi-color camERA (CHIMERA) in g and i bands in 2024 September. The CHIMERA images were corrected using bias and flat images.[20] Photometry was extracted using aperture photometry (with a variable aperture size) using a modified version of the ULTRACAM pipeline (Feline et al. 2005). We made a differential light curve using a single reference star. GPS timestamps were used to determine the mid-exposure time of each image.

A Lomb-Scargle periodogram applied to the INT i band data yielded the same period as ZTF (fourth panel in the same figure). The morphology of the phase-folded light curve also resembles that of ZTF. Owing to fewer (and denser) observations with INT g and r bands and CHIMERA, we do not apply the period search. Rather, we show the full light curves in the bottom-most panel of the same figure. The INT light curves show a flat top with pointed periodic dips, in agreement with the INT i-band and ZTF light curve shapes. But the CHIMERA light curves appear markedly different. However, we note that there were some issues with the instrument which includes it going out of focus for a while (the shaded portion), which may have degraded the quality of the data. The periodicity, however, is visually evident in the light curves.

[20] https://github.com/caltech-chimera/PyChimera

3.2.2. Discussion

Ellipsoidal modulation or irradiation effect in a binary can result in the long-period variability. The systems can also be similar to LoTr 5, where the long-term photometric modulation is suspected to arise from stellar surface activity of a giant companion phased with the orbit (Kővári et al. 2019). This is reinforced by the fact that the variability amplitudes of our objects are similar (slightly larger) to that of LoTr 5. In all of these cases, the orbital period is directly related to the photometric period (equal or double). These make both NGC 6905 and Kn 26 additional candidates for long-period wide binary CSPNe.

The light curves also bear a resemblance to Long Secondary Period (LSP) photometric modulations observed in several RGB and post-AGB stars (for example, see Kiss et al. 2006, Nicholls et al. 2009, and Soszyński et al. 2021, though the amplitudes are usually larger than seen in our targets.). This phenomenon is not yet well understood. But wide binarity and phase-dependent dust occultation (similar to RVb systems) is one proposed explanation. Here, too, the period corresponds to the binary orbital period.

We now discuss two possibilities where the long period does not correspond to the orbital period, still requiring binarity. Magnetic activity cycles of giant stars in close binaries (RS CVn systems) often result in long quasi-periodic photometric modulation. However, the associated periods are usually much longer ($\gtrsim$5 yr, see Martínez et al. 2022) than seen in NGC 6905 and Kn 26. Thus, this scenario is unlikely. The other possibility is stellar pulsations of giant stars, which is another widely accepted explanation for LSPs. Pawlak (2021) showed that LSPs tend to be stars in the RGB or AGB phase, transitioning between period-luminosity sequences.

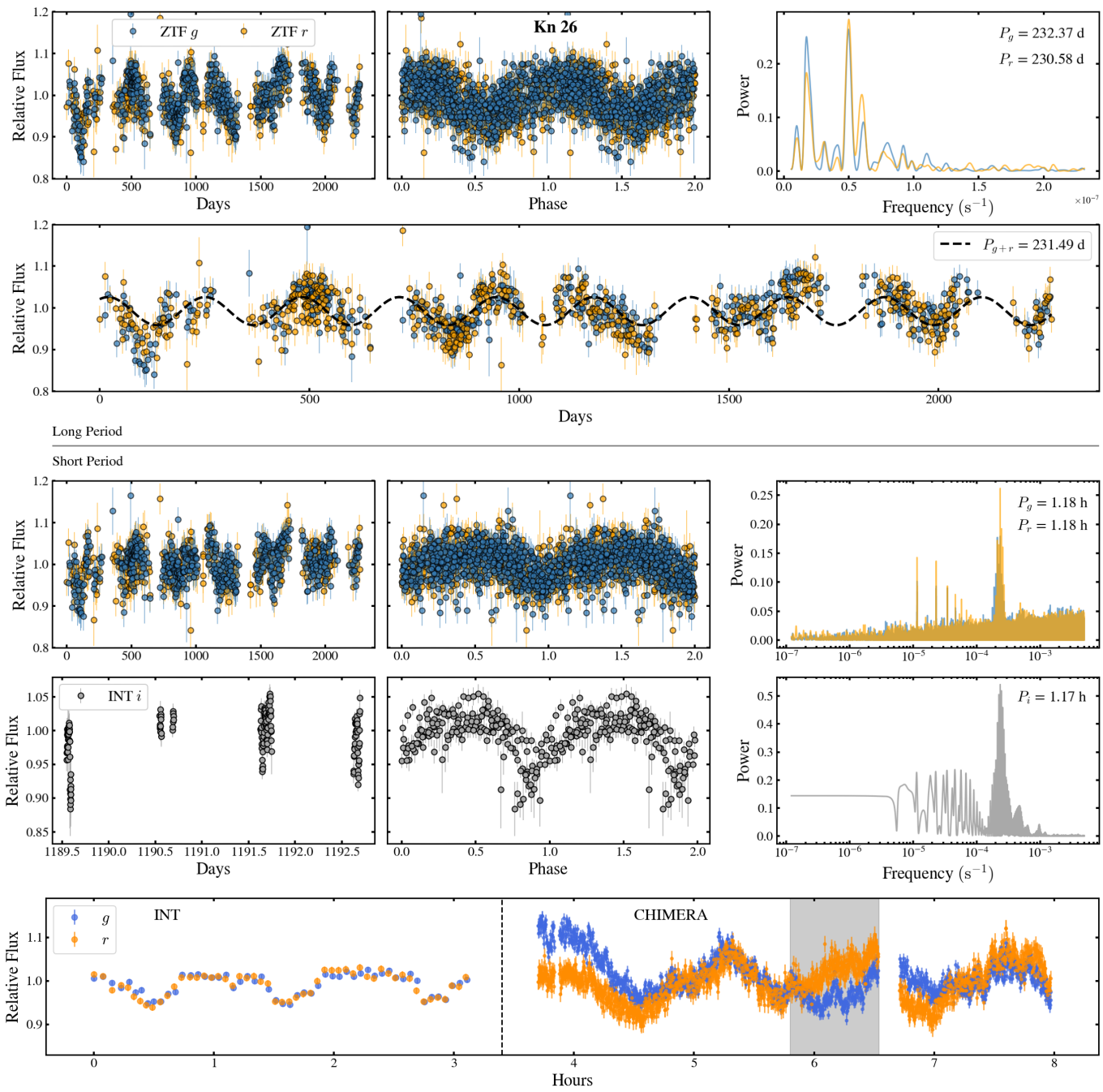

Figure 4. Periodicity in Kn 26. The long period is presented in the upper section in the same format as Figure 3. The lower section presents the short period. The three panels in this section are as follows. Top panel, from the left: ZTF light curve with the long-period normalized, phase-folded at the best period (1.18 hr), and the corresponding Lomb-Scargle Periodogram. Middle panel: Same format as the middle panel with the INT *i*-band light curve. Bottom panel: The INT and CHIMERA *g*- and *r*-band light curves. For the latter, the shaded region represents the duration for which the instrument went out of focus. The reason for the between the light curves from the two instruments is unknown, but may very well be the result of suboptimal CHIMERA observations.

Thus, with a twin-binary (El-Badry et al. 2019) setup it is possible that the companion of the CSPN is a pulsating LSP. High resolution radial velocity measurements is required to distinguish between the different scenarios.

The short period of 1.18 hr can arise from rotational modulation of the white dwarf (Oliveira da Rosa et al. 2024). Another more exotic, but unlikely, possibility (also mentioned in C25) is a close binary (this, with the long periods, may

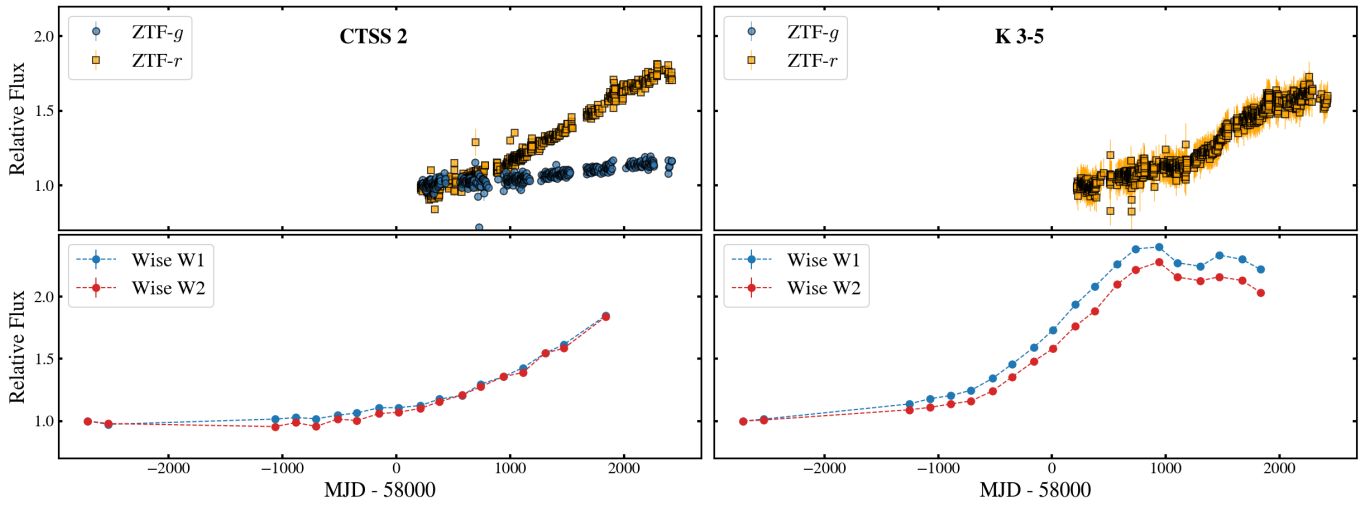

Figure 5. The ZTF and WISE light curves for CTSS 2 and K 3-5. Both show long-term photometric evolution, with the effect more pronounced in ZTF-*r* and the redder bands. The *g* band data for K 3-5 was rejected through the photometric quality cuts. However, manual inspection indicates a similar low amplitude trend as CTSS 2. For the details and discussion on these objects, see Section 3.3.

indicate a triple system!). The phase folded light curve is characterized by "pointed" minimas, morphologically similar to ellipsoidal variability with grazing eclipses. In that case, the orbital period is 2.36 hr, making it the candidate for the shortest known CSPN binary period. At such short periods, for typical stellar parameters, we expect a large radial velocity variation of $\gtrsim$100 km s^{-1}. This should be detectable. The LBT spectra at different epochs, however, do not show any radial velocity shift.

3.3. CTSS 2 and K 3-5

CTSS 2 (PN G044.1+05.8) is a True PN in the HASH catalog. The nebula is faint and can be seen only in deep narrow-band Hα images (see Figure 12.8 in Stanghellini et al. 2016 for the HST image). There has been some uncertainty in the literature regarding the true nature of the central star of CTSS 2. Stanghellini et al. (2016) note that the identified CSPN appears too bright to be associated with the faint and evolved PN, and consider the possibility of it being an unrelated field star. They also consider the possibility of it being a binary, as do Moreno-Ibáñez et al. (2016). On the other hand, García-Hernández & Górny (2014) found emission signatures unusual for a PN in the Spitzer IR spectrum, and identified CTSS 2 to be a symbiotic system candidate. Confirmatory signatures of it being either a PN or symbiotic system are, however, lacking.

K 3-5 (PN G034.3+06.2) is also a True PNe in HASH. It is a resolved bipolar nebula, with an angular diameter of 10″. The most recent spectroscopic study was performed in the spectral survey of central stars by Weidmann et al. (2018). They indicated the presence of emission lines both from the central stellar region and the extended nebula, thus making it a candidate double-envelope PN.

3.3.1. Light Curves

Figure 5 shows the ZTF and WISE light curves for CTSS 2 and K 3-5, with both objects showing very similar behavior. Over the past decade, the brightness of the objects in ZTF-*r* and the redder bands have gradually increased by a factor of ∼2. An increase in brightness in ZTF-*g* is also seen, albeit with much less prominence (flux increment by ∼30%). The light curve for K 3-5 has two additional intriguing features. First is the turnover of the WISE light curves at around MJD ∼ 58700, unlike the optical light curve. Second, a significant bluing in the WISE bands (brightening of W1 compared to W2) is seen, contrary to the behavior in the optical. In CTSS 2, the WISE bands show no significant color dependence, unlike the ZTF light curves.

3.3.2. Follow-up Optical Spectroscopy

CTSS 2 and K 3-5 were observed with the Low-Resolution Spectrograph (LRS2) on the 10 m Hobby-Eberly Telescope (HET; Ramsey et al. 1998; Hill et al. 2021) located at the McDonald Observatory in west Texas, USA, as a part of a spectroscopic survey of faint PN central stars (undertaken by H.E.B. and collaborators; see Bond et al. 2023 and subsequent papers). CTSS 2 was observed twice: 2024 September 15, 2 × 250 s, and 2024 October 15, 2 × 300 s. K 3-5 was observed once, on 2024 August 10, with a 900 s exposure.

The LRS2 instrument is described in detail by Chonis et al. (2014, 2016). Briefly, LRS2 provides integral-field-unit (IFU) spectroscopy with 280 0.″6-diameter lenslets that cover a

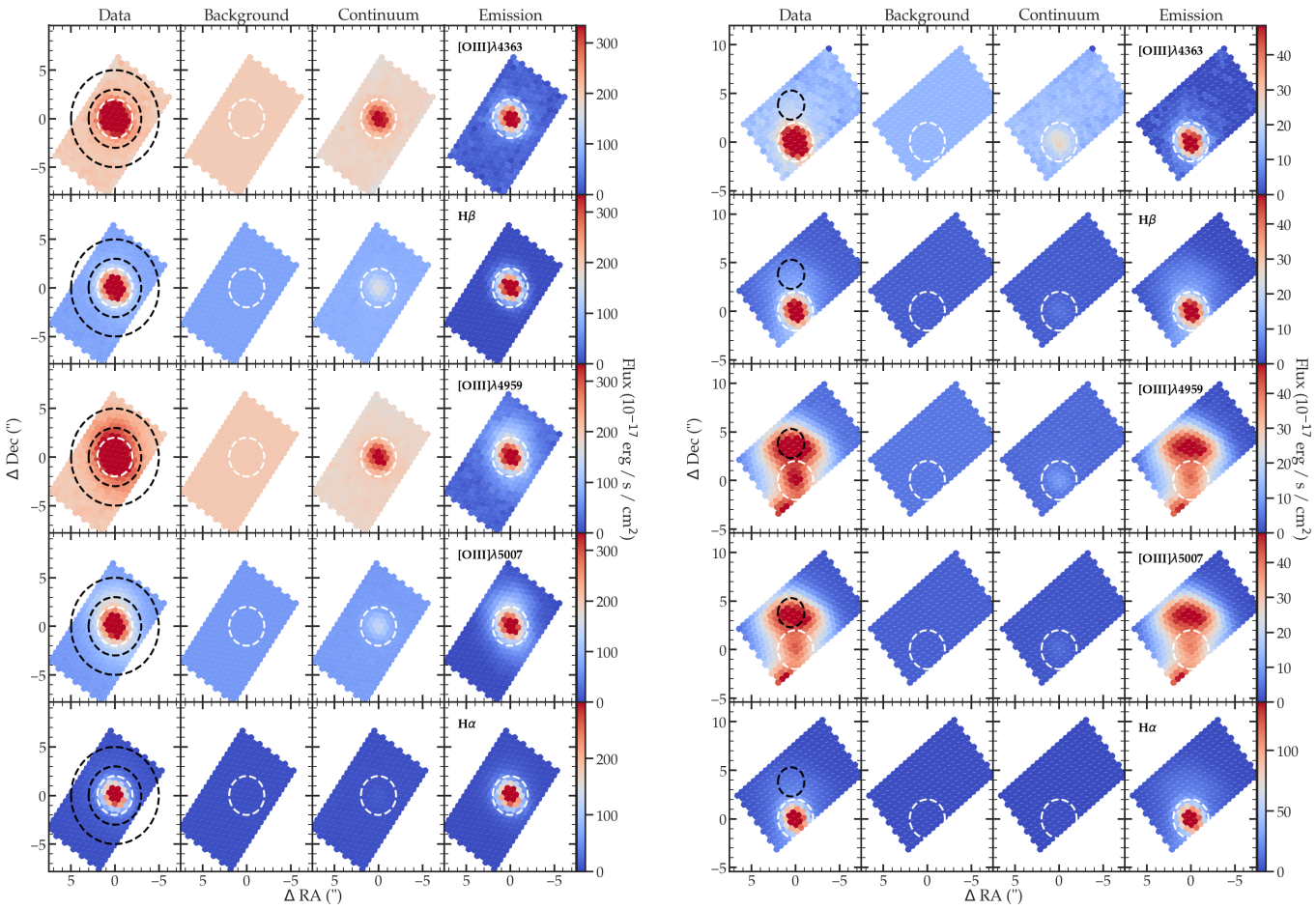

Figure 6. Synthetic narrow-band (NB, with a wavelength full-width of 16 Å) images of CTSS 2 (left panel) and K 3-5 (right panel) created from the HET LRS2-B observations around the emission lines of [O III] 4363, 4959, 5007 Å, Hα, and Hβ. The "Data" column shows the NB readings without background/nebular subtraction. The second column shows the Background modeled from fibers beyond 6.″5 from the nucleus and sufficiently away from the primary emission regions. Care has been taken to exclude the nebula from the background as much as possible. The "Continuum" column shows the stellar continuum neighboring each emission line. The final "Emission" column shows the background and continuum subtracted image, showing the emissions. The dashed white circles show the 2″ radius extraction aperture centered on the nucleus for the one-dimensional spectrum. The black annulus (for CTSS 2, 3″–5″ around the nucleus) and circle (for K 3-5, 1.″5 aperture) show the same for the corresponding nebulae. For further details on the synthesis of NB images from LRS2-B data, refer to Sections 4.1 and 4.2 in Bond et al. (2024). The central emitting core is distinctly visible against the nebula (which is diffused in case of CTSS 2 and bipolar for K 3-5). The prominence of the nebula is [O III] 4959, 5007 Å is also visible.

$12'' \times 6''$ field of view (FOV) on the sky. LRS2 is composed of two arms: blue (LRS2-B) and red (LRS2-R). All of our observations are made with the target placed in the LRS2-B FOV. The LRS2-B arm employs a dichroic beamsplitter to send light simultaneously into two spectrograph units: the "UV" channel (covering 3640–4645 Å with a resolving power of 1910), and the "Orange" channel (covering 4635–6950 Å with a resolving power of 1140). Data reduction was performed using the pipelines developed by G.R.Z.[21,22] (G. R. Zeimann et al. 2025, in preparation).

The narrow-band (NB) images for both objects around the brightest emission lines in the spectrum: Hα, β and [O III] 4363, 4959, 5007 Å are shown in Figure 6. From the two-dimensional images, one-dimensional spectra were extracted for both the central core (nucleus) and the nebula. The corresponding apertures are shown within the NB images (white and black dashed apertures correspond to the nucleus and nebula, respectively). The extracted spectra for CTSS 2 and K 3-5 are shown in Figures 7 (top panel) and 8, respectively.

Both CTSS 2 and K 3-5 were also observed with DBSP on 2024 May 13th, with exposures of 15 minutes. It is different from the HET spectrum only for its wider coverage in the red

[21] https://github.com/grzeimann/Panacea
[22] https://github.com/grzeimann/LRS2Multi

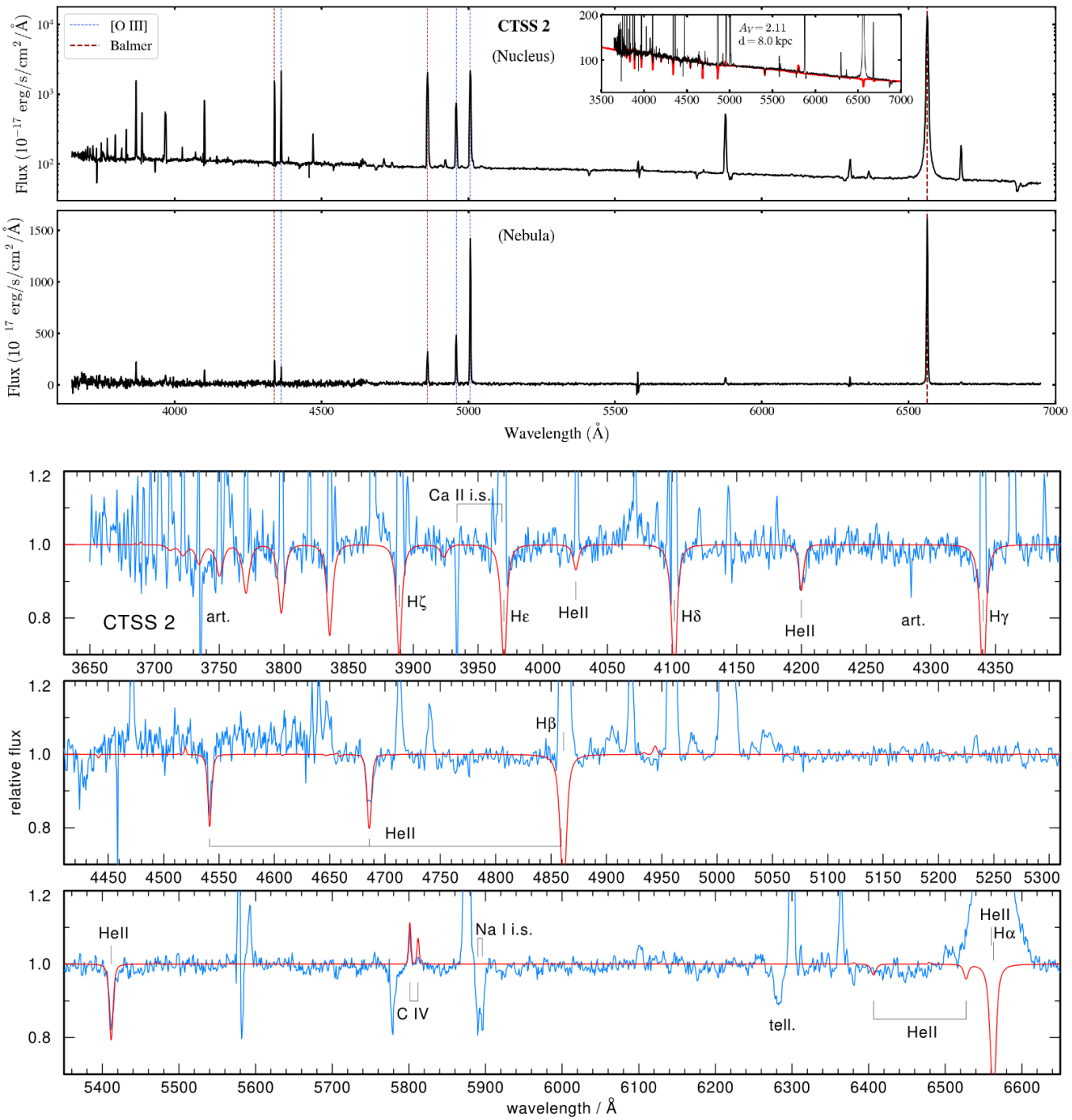

Figure 7. Upper section (two panels): One-dimensional HET spectra for the nucleus (top panel) and the nebula (bottom panel) of CTSS 2. The inset in the top panel shows the fitted stellar model compared to the un-normalized spectrum with assumed distance and extinction mentioned inside. Lower section: Model fit (red graph) to the HET spectrum of the CSPN of CTSS 2 (blue). Photospheric features are from He II, C IV, and absorption wings in the higher-order Balmer lines.

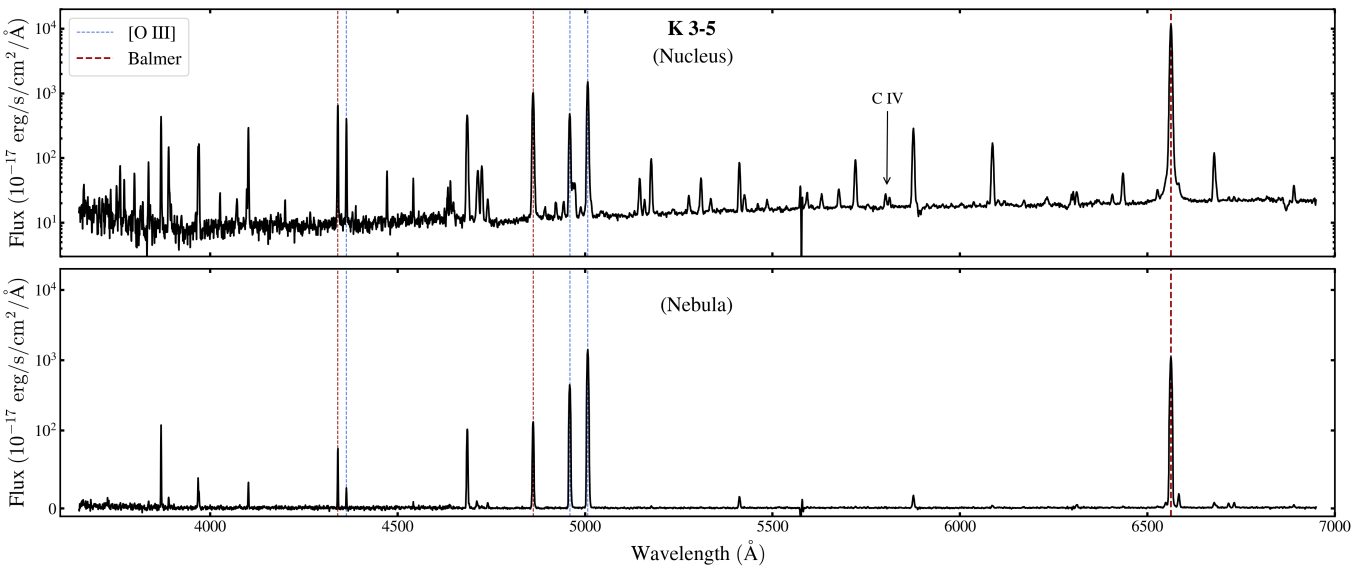

Figure 8. One-dimensional HET spectra for the nucleus (top panel) and the nebula (bottom panel) of K 3-5. The extraction fibers are mentioned in Figure 6. The C IV 5801, 5812 Å emission from the nucleus is marked.

arm. However, the HET spectrum is of higher quality and, being an IFU, enables more accurate analyses. Thus, we base our discussion on the HET spectrum in the following sections. We provide the DBSP spectrum separately in Appendix E.

3.3.3. Spectral Analysis: CTSS 2

CTSS 2 consists of a bright nucleus and a faint surrounding nebula. The left panel of Figure 6 shows the NB image of CTSS 2 around a few major emission lines. The bright core is very prominent and the faint nebula is also detected (especially in [O III] 4959, 5007 Å images). It is clear from these images that the nucleus is also very bright in the high-excitation emission lines, making it a double-envelope nebula.

We now turn to the one-dimensional spectra to understand the properties better (top panel in Figure 7). It is readily seen that the spectra (especially the relative strengths of the intensities of the major emission lines) of the nucleus and the nebula are markedly different. We now draw the attention of the readers to the strengths of Hβ and [O III] 4363 Å relative to [O III] 4959, 5007 Å. In the nucleus, we find that the intensity of Hβ is comparable to [O III] 5007 Å which is often attributed to very high electron densities. This is also supported by the high intensity of the [O III] 4363 Å emission line relative to the other [O III] lines.

To perform a more quantitative estimate, we define (as in Paper I) $O_{ratio} = \frac{\text{[O III] 5007 Å+[O III] 4959 Å}}{\text{[O III] 4363 Å}}$, which is related to the electron densities and temperatures (see Equation (3) in Paper I, taken from Osterbrock & Ferland 2006). Overall, a lower value of O_{ratio} signifies very high densities and/or temperatures. We obtain $O_{ratio} \approx 3.5$ for CTSS 2 nucleus. This value is strikingly small for a PN. With this value, any reasonable temperature would estimate electron densities of $n_e \gtrsim 10^6$ cm^{-3}. Unlike the nucleus, the nebula as a much larger O_{ratio} of ≈25.4. This is consistent with the expectation that the diffuse nebula should be significantly less dense than the core. However, this is still lower than in most PNe and indicates moderately high electron densities of $n_e \gtrsim 10^5$ cm^{-3}.

We also find evidence of fast wind/shock activity in the nucleus. The top panel of Figure 9 shows a zoom-in of the base of the Hα emission lines for both the nuclear and the nebular spectra. Broad wings extending up to velocities of $\gtrsim$1500 km s^{-1} are seen in the nuclear spectrum. In contrast, the nebular spectrum is much narrower, showing that the wind activity is mostly localized to the core. But the wings of the nebular Hα still extend up to velocities of ≈750 km s^{-1}, which might indicate an extended influence of the nuclear activity. Note that such wind/shock may heat up the environment beyond that achievable through photoionization equilibrium, and contribute to lowering the inferred O_{ratio}.

The continuum in the nuclear spectra contains absorption signatures (H and He), which we attribute to the central star. We also detect an emission doublet of C IV 5801, 5812 Å, typical of many hot stars. To infer the stellar parameters we performed a spectral fit. We computed a series of non-local thermodynamic equilibrium models of the type introduced by Werner et al. (2019) using the Tübingen Model-Atmosphere Package (Werner et al. 2003). They are plane-parallel and in radiative and hydrostatic equilibrium. They are composed of hydrogen and helium while carbon and nitrogen were included as trace elements, keeping fixed the atmospheric structure. We assumed solar composition. Models were computed in the

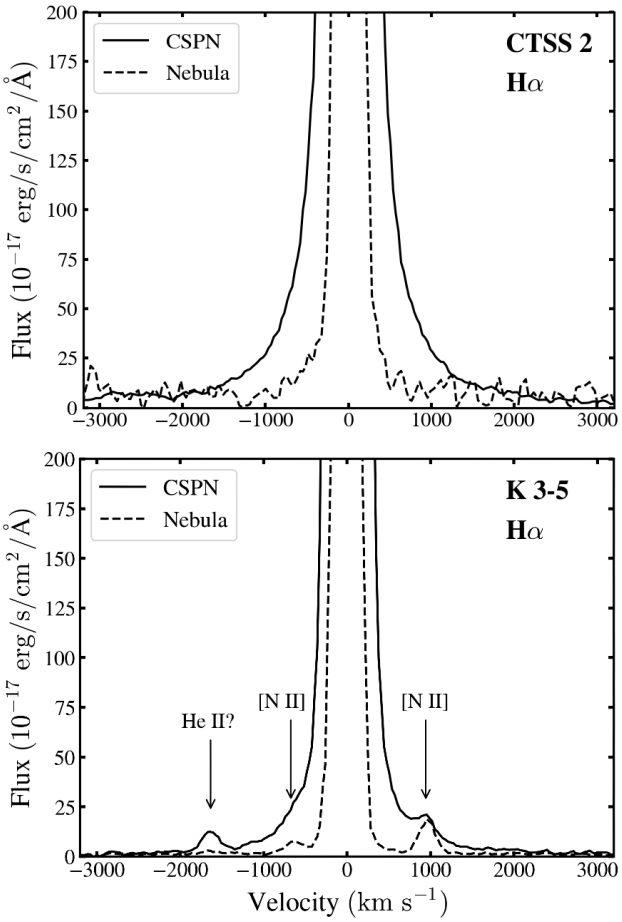

Figure 9. Zoom-in on the wings of the Hα emission line in CTSS 2 (top panel) and K 3-5 (bottom panel) for both the nucleus (solid line) and nebula (dashed line). The extended wings up to $\gtrsim$1000 km s^{-1} indicates wind/shocks. For K 3-5 the best guesses for the additional emission features are marked.

range $T_{\rm eff}$ = 50–90 kK and $\log(g/[{\rm cm\,s^{-2}}])$ = 3.9–4.8. The best-fit parameters were determined by eye and found to be $T_{\rm eff} = 70 \pm 10$ kK and $\log(g) = 4.5 \pm 0.2$ (bottom three panels in Figure 7 show the fit to the normalized spectrum). Using evolutionary tracks by Miller Bertolami (2016) this corresponds to stellar mass, radius, and luminosity of $M = 0.65^{+0.06}_{-0.03}\,M_{\odot}$, $R = 0.75^{+0.24}_{-0.17}\,M_{\odot}$, and $\log(L/L_{\odot}) = 4.08^{+0.48}_{-0.48}$. The corresponding age of the central star is inferred to be $\approx$1500 $\pm$ 500 yr. This makes it a candidate for one of the youngest post-AGB phase CSPN. We comment here on the possible "contamination" from any nebular continuum. We do not expect significant contamination from the faint diffused nebula, but any continuum associated with the central emitting core can potentially dilute the absorption lines, rendering the spectral fit suboptimal. As this emission is mostly unresolved, appropriate modeling of the emission lines is needed to correct for any such contamination. Such a detailed study is beyond the scope of this paper.

The Gaia parallax distance to CTSS 2 is $d = 8.77^{+6.97}_{-2.69}$ kpc. The analysis of Bailer-Jones et al. (2021) yields a slightly different distance estimate of $6.63^{+1.81}_{-1.47}$ kpc. We use the inferred stellar parameters to get an independent estimate of the distance to CTSS 2. We first employ a simple manual comparison of the model to the observed spectrum, by varying the reddening and the distance. A good visual fit was obtained with E_{B-V}= 0.68 (i.e. $A_V = 2.11$) and $d = 8.0$ kpc (see inset in the top panel of Figure 7).[23] The distance is consistent with the Gaia distances.

The extinction value used above is consistent with that inferred from the Balmer line ratios. We first use the nebular spectrum to estimate A_V. Following the same strategy as in Paper I, we get $\mathrm{BD}_{\alpha\beta} = 6.13$ (the ratio of Hα to Hβ) and $\mathrm{BD}_{\beta\gamma} = 2.85$ which leads to extinction estimate of $A_V = 2.12 \pm 0.02$. For the nuclear spectrum, we obtain $\mathrm{BD}_{\alpha\beta} = 8.71$ and $\mathrm{BD}_{\beta\gamma} = 2.98$ which translates to $A_V = 2.7 \pm 0.3$. This is slightly higher than the nebular estimate but broadly consistent.

From the HST image in Stanghellini et al. (2016), we estimate the angular diameter of the nebula to be around 7″. Assuming a distance to the nebula of 8 $\pm$ 2 kpc, gives the physical radius of the nebula is $\approx$0.13 $\pm$ 0.03 pc. This gives an average expansion speed of $\approx 88^{+78}_{-40}$ km s^{-1}. This is marginally higher than the average expansion velocities of PNe ($\approx$40 km s^{-1}, Jacob et al. 2013; Pereyra et al. 2013), but consistent within the error limits.

3.3.4. Spectral Analysis: K 3-5

The right panel in Figure 6 shows the narrow band images on K 3-5. It is quite intriguing to observe that the nucleus is brighter than the nebula in Balmer and [O III] 4363 Å emissions, however, the reverse is true for [O III] 4959, 5007 Å images.

We proceed to perform a similar analysis as with CTSS 2 with the one-dimensional spectra (Figure 8): comparing the nuclear and nebular spectra and inferring the physical properties. The strengths of the emission lines are different between the nucleus and the nebula in a very similar way as in CTSS 2. The increased strength of the Hβ and [O III] 4363 Å emission lines indicate a double envelope nature of the PN with a localized high-density emission core. This is in line with the inferences in Weidmann et al. (2018).

For the nebular spectrum, we get $\mathrm{O}_{\rm ratio} \approx 158$. This is at par with the typical values for evolved PNe. Additionally, [S II] 6716, 6731 Å lines are prominently detected in the spectrum. We obtain an intensity ratio of [S II] 6716/[S II] 6731 = 0.91. These two line ratios combined (from Osterbrock & Ferland 2006) yield electron densities of $n_e \approx 700$ cm^{-3} and temperature of $T_e \approx 11$ kK. These properties are consistent with that of a PN.

[23] All dust extinction corrections in this work have been performed using the `dust_extinction` (Gordon 2024a, 2024b) implementation of the Gordon et al. (2023) galactic extinction models (Gordon et al. 2009; Fitzpatrick et al. 2019; Gordon et al. 2021; Decleir et al. 2022).

For the nucleus, however, we derive a significantly lower O_{ratio} of ≈11. For any temperature, this yields $n_e > 10^5\,cm^{-3}$, significantly higher than the inferred nebular density, in line with it being a high-density emission core. We note here that weak [S II] lines are also detected in the nuclear spectrum, bearing a similar intensity ratio as the nebula. This is inconsistent with the low O_{ratio} value. We thus conclude that this is just a contamination in the nuclear aperture from the overlapping nebula. Unlike CTSS 2, no absorption signature from the central star is detected in the nuclear spectrum, preventing any parameter estimation of the CSPN. However, certain emission lines might arise from the central stellar system. For example, we detect C IV 5801, 5812 Å emission line in the nuclear spectrum (absent in the nebular spectrum). This doublet is often associated with either the photosphere of a hot CSPN (like CTSS 2) or an irradiated companion.

Like CTSS 2, K 3-5 also has broad Hα emission wings in the nuclear spectrum, extending up to velocities of $\gtrsim$1000 km s^{-1} (bottom panel of Figure 9). On the other hand, the nebula profile is much narrower, it's width probably being just limited by the instrument resolution. Note that faint [N II] 6548, 6583 Å are detected in both the nuclear and the nebular spectra (marked in the figure, though we suspect the former to be just nebular contamination like the [S II] lines). In the same figure, we see an emission signature at ≈−1500 km s^{-1} in the nuclear spectrum. This can be the He II 6527 Å line corresponding to the $n = 14$ to $n = 5$ transition (see for example Lee et al. 2001).

We infer a very high reddening for this object. We infer $BD_{\alpha\beta} = 13.7$ and $BD_{\beta\gamma} = 3.4$ from the nuclear spectrum. The nebular spectrum also yields consistent values of 9.96 and 3.67 respectively. This translates to $A_V \approx 3.7 \pm 0.4$. This explains the apparent red continuum of the nuclear spectrum. We note that such a high reddening revises the inferred values of O_{ratio} for the nucleus and the nebula to ≈6 and ≈82. None of our conclusion changes because of this, apart from increasing the density estimation for the nucleus to $n_e \gtrsim 10^6\,cm^{-3}$.

3.3.5. Discussion

CTSS 2 is a good candidate for a late thermal pulse (LTP) scenario, in which the star experiences a late He-shell flash shortly after leaving the AGB (e.g. Lawlor 2023). LTPs are expected to occur frequently, and lead to an accelerated evolution of the star. Thus far, only two such stars have been "caught in the act": SAO 244567 was observed during the initial rapid heating and contraction, which was followed around 2002 by a rapid cooling and expansion of the star Reindl et al. (2014, 2017). The other example is FG Sge which was observed only during the cooling and expansion phase, returning to the AGB, where it turned into an H-deficient now an RCB star (Jeffery & Schönberner 2006). We stress that the brightening rate of CTSS 2 is very similar to that of FG Sge (see, for example, Figure 3 in van Genderen & Gautschy 1995), and the strong reddening observed in the light curves of CTSS 2 suggests that the star is currently cooling. (Jeffery & Schönberner 2006) explained the evolution of FG Sge with a 0.625 $M_\odot$ LTP model, which agrees very well with our inferred mass of the CSPN of CTSS 2. We also note that the H-rich surface composition of CTSS 2 is what is expected from LTP models before the star manages to evolve back to the AGB (e.g. Lawlor 2023) and what was observed for SAO 244567 and FG Sge. K 3-5 might also be an LTP candidate, given the similarity in light curve behavior. But without any spectroscopic identification of the CSPN, the inference is more uncertain.

We now consider a few other possible scenarios. Firstly, we deem it unlikely that the observed light curves are part of a periodic binary signal. The lack of turnover in the light curves implies $P \gtrsim 15$ yr. At such a wide orbit, neither irradiation nor ellipsoidal variability can be strong enough to cause the observed brightening. The former might be significant for a highly eccentric orbit, but the duration of the periastron (thus the irradiation effect) then would be much smaller. Thus, we deem this scenario highly unlikely.

The two systems can be similar to IC 4997, which shows decades-long photometric evolution comprising of both dimming and brightening episodes (Aller & Liller 1966; Kostyakova & Arkhipova 2009; Arkhipova et al. 2020). The cause for the variability is yet unclear. The other possibility is long-term dust activity, as witnessed in M 2-29 (Hajduk et al. 2008; Miszalski et al. 2011b). The spectral energy distributions of both CTSS 2 and K 3-5 indeed indicate the presence of a large amount of dust (see Appendix F). Long-term photometric and spectroscopic[24] monitoring is needed for a more concrete understanding of these systems.

The high-density emission cores in both systems warrant a separate mention. This is a property of the so-called EGB 6-type PNe (Liebert et al. 2013) bearing Compact Emission Knots (CEKs), hypothesized to be an irradiated dense accreted envelope around a wide-orbit companion to the CSPN white dwarf. Thus, this may be an indirect indication of the binarity of the CSPNe. For K 3-5, the bipolar nature of the nebula also supports multiplicity of the CSPN. Another explanation involving a companion might be a symbiotic interaction, where such high density cores are common. The lack of the spectral signatures of a Mira giant in the red end (see the DBSP spectrum with a better red coverage, Figure E1), however, speaks against them being the more common D-type

[24] Comparison of the current and past spectra indeed indicates spectroscopic evolution of both CTSS 2 and K 3-5. The spectra of both of them on HASH (and in Stanghellini et al. (2016) for CTSS 2) has Hβ strength much less than the neighboring [O III] lines, and a weak [O III] 4363 Å. This might indicate an increase in n_e associated with the brightening. But we do not establish it with confidence because of a lack of knowledge about the details of the archival spectra (trace selection, nucleus versus nebula).

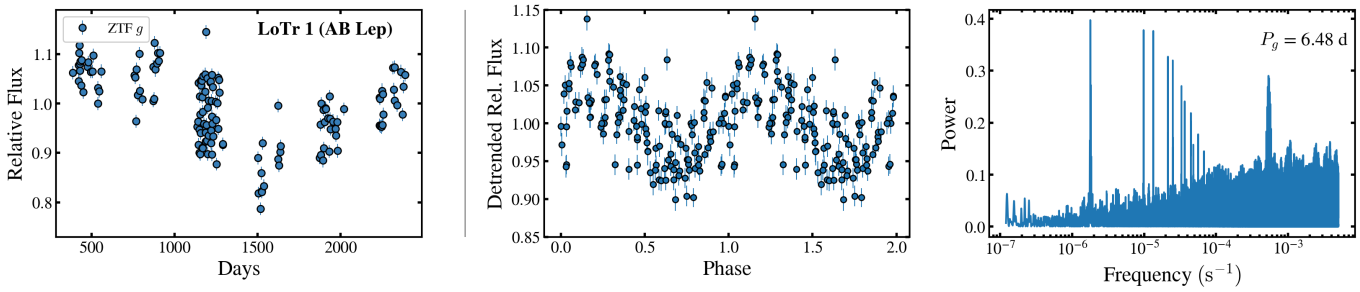

Figure 10. Variability in LoTr 1. Left: The raw ZTF light curve. Middle: Season-wise de-trended ZTF light curve phase folded to its best period. Right: The periodogram for the de-trended ZTF data and the best period.

symbiotic system. They can be the less common S or D'-type symbiotics. The presence of these systems inside PNe are rare. Confirmatory signatures of symbiotic behavior, like the Raman-scattered O VI emissions, are not seen in the spectra. But this does not rule out symbiotic interaction as such signatures are highly variable and not present in many systems.

3.4. LoTr 1

LoTr 1 is a True PN in HASH and has a diameter of 145″. Its CSPN, AB Lep, is a known variable.

3.4.1. Light Curves

Long-term photometric modulation was reported in Martínez et al. (2022), with a period of 11.28 yr. They present LoTr 1 as a RS CVn system: a close binary with a giant companion where the magnetic activity cycle of the giant star leads to long-period photometric variability. On short timescales, it shows a period of 6.4 days, which has been attributed to the rotation of the giant star (Tyndall et al. 2013).

The ZTF light curve shows a long-lasting "dip" (left panel in Figure 10). This is likely a segment around the minimum of the longer periodic variability (the time of the minima and the amplitude are consistent with that expected from Martínez et al. 2022). We successfully recover the signal in the season-wise de-trended ZTF light curve (the right two panels in the same figure) as the dominant periodogram peak. Note that C25 also detected this period, but, unlike this work, it did not appear as their dominant peak (their Figure 14).

We note that LoTr 1 is similar to LoTr 5, which consists of an unresolved hot (pre-)white dwarf and rapidly rotating magnetically active G5 giant pair. For the latter system Kővári et al. (2019) uncovered a long-term photometric variability which appears in phase with the orbital radial velocity of the binary ($P_{\rm orbit} \approx 7.4$ yr). Thus, one can likewise speculate that the long-term variability in LoTr 1 might reflect the orbital period of the binary system. Unlike Martínez et al. (2022), we propose that this is a wide binary with a rapidly rotating giant companion.

3.4.2. HST/COS Spectroscopy and Spectral-Energy Distribution

The central star of LoTr 1 was observed for 2299 s on 2023 March 29, with the Cosmic Origins Spectrograph (COS) aboard the Hubble Space Telescope (HST), using the G130M grating centered on 1291Å (data set LEZCI2020, PI: N. Reindl). Another 1640 s exposure was taken with HST/COS on 2023 July 30, using the G140L grating ($R \approx 1000$) that covers ≈1150–1700 Å (data set LEZCI5010, PI: N. Reindl). The spectra were retrieved from the MAST archive.

The hot central star of LoTr 1 turns out to be a spectroscopic twin of the extremely hot white dwarf in UCAC2 46706450 (Werner et al. 2020) as it becomes obvious when looking at Figure 11 where we compare the UV spectra of both stars. The lack of observed Fe V lines as well as the absence of the C III multiplet at 1175 Å imposes a lower $T_{\rm eff}$ limit of 100,000 K (Werner et al. 2020). In the G140L spectrum, a weak He IIλ 1640 Å can be detected which suggests that the central star of LoTr 1 is either a very hot DAO white dwarf or a O(H)-type pre-white dwarf. Interestingly, the companion of UCAC2 46706450 is also a rapidly rotating giant star.

In order to estimate the radii of both stars we carried out a two-component fit to the spectral energy distribution (SED) of LoTr 1, employing the χ^2 SED fitting routine described in Heber et al. (2018) and Irrgang et al. (2021). For the cool star we used PHOENIX models calculated by Husser et al. (2013) and for the hot central star the metal free model grid computed by Reindl et al. (2023). We fixed the $T_{\rm eff}$ of the central star to 105,000 K (i.e. to the value that was derived for UCAC2 46706450 by Werner et al. 2020), and then let the let the angular diameter, reddening, surface ratio of both stars, as well as the $T_{\rm eff}$ of the cool companion vary freely. The resultant fit is shown in Figure 12. We derive a reddening of $E(44–55) = 0.08$ mag[25] and a radius of 0.44 $R_\odot$ for the hot central star (identical to UCAC2 46706450), indicating that it

[25] Fitzpatrick et al. (2019) employs $E(44–55)$, which is the monochromatic equivalent of usual $E(B-V)$, using the wavelengths 4400 Å and 5500 Å, respectively. For high effective temperatures such as for the stars in our sample $E(44-55)$ is identical to $E(B-V)$.

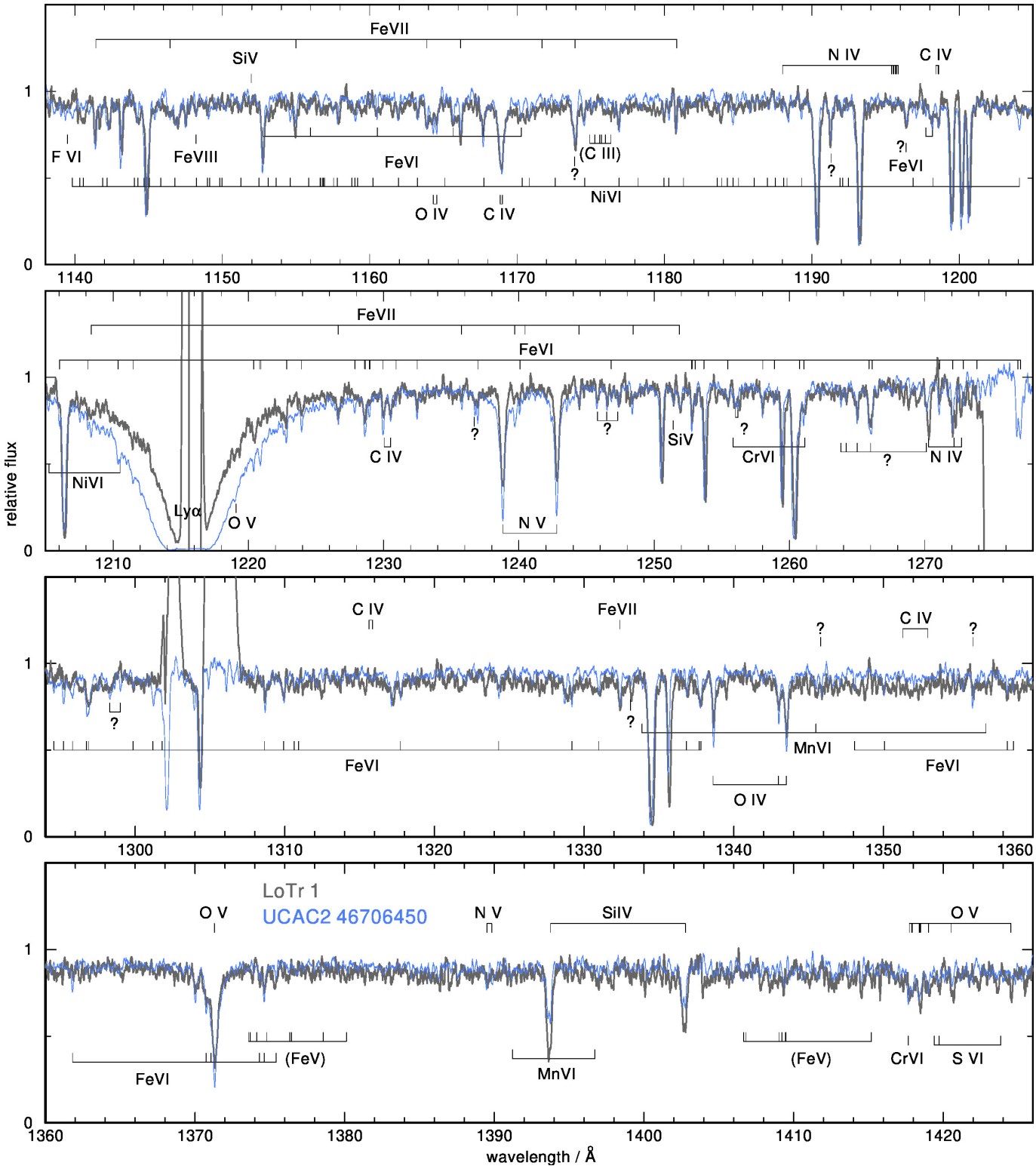

Figure 11. HST/COS G130M spectrum of the LoTr 1 (gray) compared to the HST/COS G130M spectrum of its spectroscopic twin, the very hot white dwarf in UCAC2 46706450 (blue graph). The spectra were smoothed with a 0.1 Å wide boxcar to increase the signal-to-noise ratio. Prominent photospheric lines are identified. Identifications in brackets denote uncertain detections. Question marks indicate unidentified photospheric lines.

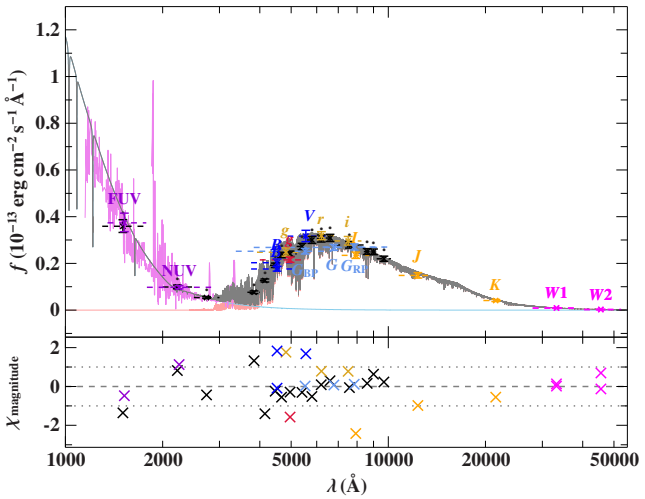

Figure 12. Top panel: SED fit for LoTr 1. Filter-averaged fluxes converted from observed magnitudes are shown in different colors. The respective full width at tenth maximum are shown as dashed horizontal lines. In pink the spectrum from the International Ultraviolet Explorer is shown. The combined best-fitting model, degraded to a spectral resolution of 6 Å is plotted in gray. The blue graph represents the model for the hot central star and the salmon graph is the model for the cool giant. Bottom panel: the difference between synthetic and observed magnitudes.

is just about to enter the white dwarf cooling sequence. For the cool giant star we derive $T_{\rm eff} = 4590$ K and a radius of 9.7 $R_{\odot}$. These parameters are broadly consistent with a subgiant star of mass in the range of $\approx$1–2 $M_{\odot}$,[26] which is also very similar to the companion of UCAC2 46706450. With the 6.48 days rotational period, this implies a surface velocity of 75 km s^{-1}.

3.5. The Other Long-timescale Variables

In this section, we briefly introduce the remaining five long-timescale variables. Further spectroscopic and photometric studies of these objects are underway and will be presented in future works. The ZTF light curves are shown in Figure 13. Except for Kn J1857.7+3931 (henceforth, Kn J1857) and IPHAS J192717.94+081429 (henceforth, IPHAS J1927), all of the long-timescale variables are True PN on HASH with resolved nebulae. Kn J1857 has now been reclassified to "object of unknown nature" on HASH, and IPHAS J1927 is a Possible PN. Neither of the two has a resolved nebula (thus either a very young PNe or some stellar PN mimic).

We first discuss the True PNe. K 3-20 shows a brightening event, with a larger amplitude in the ZTF r band. Tan 2 shows a singular eclipse-like dip in the g band. Unfortunately, the r band data for this object did not pass the photometric quality cuts. The light curve of WHTZ 3, albeit noisier, shows low-amplitude

[26] We compared the stellar parameters to Modules for Experiments in Stellar Astrophysics (MESA, Paxton et al. 2011, 2013, 2015) evolutionary tracks queried from MESA Isochrones and Stellar Tracks (MIST, Dotter 2016; Choi et al. 2016). Owing to the preliminary nature of the analysis we do not show the comparison. This will be presented elsewhere with spectroscopic observations.

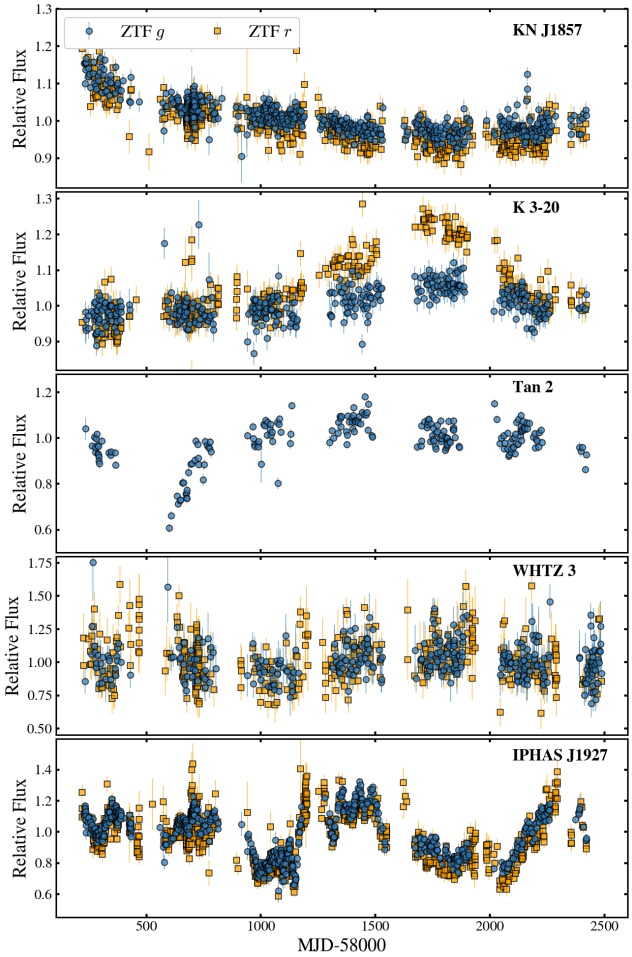

Figure 13. The light curves for the remaining five long-timescale variables within the HNEV sample. A brief discussion on these objects is presented in Section 3.5.

long-term modulation. The possible causes for variability of these objects are uncertain. The observed light curves can be a part of even longer timescale periodic variability associated with binarity. For example, the behavior in K 3-20 may result from irradiation effect in a long-period wide binary (similar to NGC 6833). Further long-term photometric monitoring is needed to test these scenarios. Concerning the remaining two objects, Kn J1857 shows a gradual dimming by $\sim$25% in flux, with similar amplitude in both the ZTF bands. The variability in IPHAS J1927, on the other hand, is more irregular. Similar kinds of photometric behaviors are often seen in symbiotic systems or cataclysmic variables (CVs). Being only a "Possible PN," spectroscopic data are necessary to determine the true nature of this object.

4. Summary and Conclusions

This is the second in a series of papers undertaking a systematic study of the variability of central stars of planetary nebulae (CSPNe), using optical light curves from the Zwicky

Transient Facility (ZTF). In Paper I, we applied appropriate variability metrics to identify significantly variable sources. The present paper reports the 11 objects that show long-timescale variability. For six of these objects, we present follow-up spectroscopic/photometric observations and provide extensive discussion, which is expected to serve as the first step in understanding the objects. We also present the remaining six objects and encourage follow-up studies by the community.

The first object we discuss is NGC 6833 (Section 3.1). It shows "triangle-shaped" brightening in the ZTF *r*, *i*, and WISE W1 and W2 bands, occurring at a period of ∼980 days. The more intriguing aspect is the anti-correlated behavior in the ZTF *g*-band, which shows shallow dips nearly at the same epochs as the peaks in the redder bands. We think that this is a long-period eccentric binary, with the photometric period corresponding to the orbital period. This makes it the candidate for the fourth-longest binary orbital period inside a PN. Though the irradiation effect can possibly explain the brightening, the simultaneous dips in *g*-band is puzzling. Dust occultation and extinction can potentially result in such a feature.

Long-periodic modulation was also detected in the light curves of NGC 6905 and Kn 26 (Section 3.2). The former showed a significant peak at ∼700 days and the latter at 230 days. Secondary significant peaks were also detected at ∼245 days and ∼630 days. The modulation appears broadly sinusoidal. This makes both the objects candidates for long-period binary CSPNe. Kn 26 displays an additional periodicity at 1.18 hr, which we verify through follow-up photometry. The origin of this period is uncertain. It can be due to a close binary (unlikely) or rotational origin.

We present CTSS 2 and K 3-5, which show slow and long-term brightening (Section 3.3). The objects brightened by almost a factor of 2 in the ZTF *r*-band and WISE bands, but much less so (factor of $\lesssim$1.25) in the *g*-band, thus undergoing significant reddening. Spectroscopy of both the nucleus and the nebula shows that both objects host high-density ($n_e \gtrsim 10^6\,\mathrm{cm}^{-3}$) emission-line cores. Thus they are either EGB 6-type PNe with compact emission knots, or symbiotic systems. The optical spectrum of CTSS 2 displays stellar absorption signatures. A spectral fit yields a temperature of 70 kK and a stellar mass of 0.65 $M_\odot$. This translates to a post-AGB age of ≈1500 yr, making it one of the youngest CSPNe known. Unfortunately, the spectrum of K 3-5 does not show adequate stellar features, thus preventing any spectroscopic analysis of the (pre-)white dwarf. We think that these might be late thermal pulse events. In this case, the light curves suggest that the stars are cooling down and expanding, moving back to another AGB phase. This is a very rare occurrence and would indicate the success of long-baseline surveys like ZTF to discover these objects. Other possible explanations include wind/dust activity of the CSPN system.

We present new results on LoTr 1 (Section 3.4), which is a known variable showing a long-period modulation at $P = 11.28$ yr and a shorter period at 6.5 days. The latter is attributed to the rotational modulation of a fast-rotating cool giant companion. The longer period might be the orbital period. Ultraviolet spectroscopy with HST shows that the hot component in the system is a spectroscopic twin of the extremely hot white dwarf in UCAC2 46706450, with a temperature of 105 kK. A fit to the SED reveals the stellar parameters of the giant to be $T_{\rm eff} = 4590$ K and radius of $R = 9.7\,R_\odot$.

Finally, we briefly discuss the observed variability in the remaining five objects (Section 3.5). They display a variety of photometric behaviors: long-timescale dimming, single brightening event, single dip event, or more erratic variability. Follow-up studies are necessary to understand these systems.

Overall, this study shows the effectiveness of long-baseline surveys in uncovering the variety of photometric behaviors observed in CSPNe. Efforts need to be made not only to understand the objects individually through follow-up observations, but, if possible, to establish evolutionary links to different classes of objects. For example, the peculiar photometric behavior of NGC 6833 may shed significant light on the formation and evolution of post-CE wide binary systems. Note here that ZTF can only access the northern sky. The majority of PNe are in the southern sky, near the Galactic center. Upcoming surveys like LSST will observe these targets, and we expect to find several more such intriguing systems. Simple variability metrics and metric spaces (as demonstrated in Appendix A) will significantly boost such discoveries.

Acknowledgments

This work is based on observations obtained with the Samuel Oschin Telescope 48 inch and the 60 inch Telescope at the Palomar Observatory as part of the Zwicky Transient Facility project. ZTF is supported by the National Science Foundation under grant Nos. AST-1440341 and AST-2034437 and a collaboration including current partners Caltech, IPAC, the Oskar Klein Center at Stockholm University, the University of Maryland, University of California, Berkeley, the University of Wisconsin at Milwaukee, University of Warwick, Ruhr University Bochum, Cornell University, Northwestern University, and Drexel University. Operations are conducted by COO, IPAC, and UW.

This work has made use of data from the European Space Agency (ESA) mission Gaia (https://www.cosmos.esa.int/gaia), processed by the Gaia Data Processing and Analysis Consortium (DPAC; https://www.cosmos.esa.int/web/gaia/dpac/consortium). Funding for the DPAC has been provided by national institutions, in particular, the institutions participating in the Gaia Multilateral Agreement.

We are grateful to the staffs of Palomar Observatory and the Hobby-Eberly Telescope for assistance with the observations and data management. The Liverpool Telescope is operated on the island of La Palma by Liverpool John Moores University in the Spanish Observatorio del Roque de los Muchachos of the Instituto de Astrofisica de Canarias with financial support from the UK Science and Technology Facilities Council.

The Low-Resolution Spectrograph 2 (LRS2) on HET was developed and funded by the University of Texas at Austin McDonald Observatory and Department of Astronomy, and by Pennsylvania State University. We thank the Leibniz-Institut für Astrophysik Potsdam (AIP) and the Institut für Astrophysik Göttingen (IAG) for their contributions to the construction of the integral field units. We acknowledge the Texas Advanced Computing Center (TACC) at The University of Texas at Austin for providing high performance computing, visualization, and storage resources that have contributed to the results reported within this paper.

The Isaac Newton Telescope is operated on the island of La Palma by the Isaac Newton Group of Telescopes in the Spanish Observatorio del Roque de los Muchachos of the Instituto de Astrofísica de Canarias

S.B. thanks Frank J. Masci and Zachary P. Vanderbosch for useful discussions and suggestions regarding solving the issues with ZTF forced photometry on extended sources. S.B. also thanks Jim Fuller, Charles C. Steidel, Lynne Hillenbrand, and Adolfo Carvalho for useful discussions on methods and science. S.B. acknowledges financial support from the Wallace L. W. Sargent Graduate Fellowship during the first year of his graduate studies at Caltech. N.C. was supported through the Cancer Research UK grant A24042.

N.R. is supported by the Deutsche Forschungsgemeinschaft (DFG) through grant RE3915/2-1.

D.J. acknowledges support from the Agencia Estatal de Investigación del Ministerio de Ciencia, Innovación y Universidades (MICIU/AEI) under grant "Nebulosas planetarias como clave para comprender la evolución de estrellas binarias" and the European Regional Development Fund (ERDF) with reference PID-2022-136653NA-I00 (DOI:10.13039/501100011033). D.J. also acknowledges support from the Agencia Estatal de Investigación del Ministerio de Ciencia, Innovación y Universidades (MICIU/AEI) under grant "Revolucionando el conocimiento de la evolución de estrellas poco masivas" and the the European Union NextGenerationEU/PRTR with reference CNS2023-143910 (DOI:10.13039/501100011033).

We have used `Python` packages Numpy (Harris et al. 2020), SciPy (Virtanen et al. 2020), Matplotlib (Hunter 2007), Pandas (pandas development team 2020), Astropy (Astropy Collaboration et al. 2013, 2018), and Astroquery (Ginsburg et al. 2019) at various stages of this research.

Appendix A
The Von-Neumann and Pearson Skew Metric Space

In Appendix B of Paper I, we presented a two-dimensional metric space defined by the variability metrics von Neumann statistics and Pearson Skew (vonN and SkewP, Equations (B1) and (B2) in Paper I respectively). We demonstrated the ability of the metric space to identify "uniquely" variable light curves, like WeSb 1, from a larger pool of objects. We briefly review the metric space and its functionality. The Vonn metric quantifies the randomness in the time-series data. Theoretically, an adequately sampled completely random data should have vonN $\sim$2 (von Neumann 1941). SkewP, on the other hand, quantifies the directionality of the variability ($<$0 signifies dips/eclipses, and $>$0 indicates outbursts). Non-variable sources with just photon shot noise, thus, cluster around vonN $\sim$2 (slightly lower at $\sim$1.8 in practice) and SkewP $\sim$ 0.

In Paper I, we discussed the position of the short-timescale variables in this metric space. We now focus on the long-timescale variables. Figure A1 is the same as Figure B1 in Paper I with all the 11 long-timescale variables marked individually. The notable feature is that almost all the sources (except WHTZ 3, where the light curve is noisier) have low values of the Vonn metric ($<$1). This is because the variability

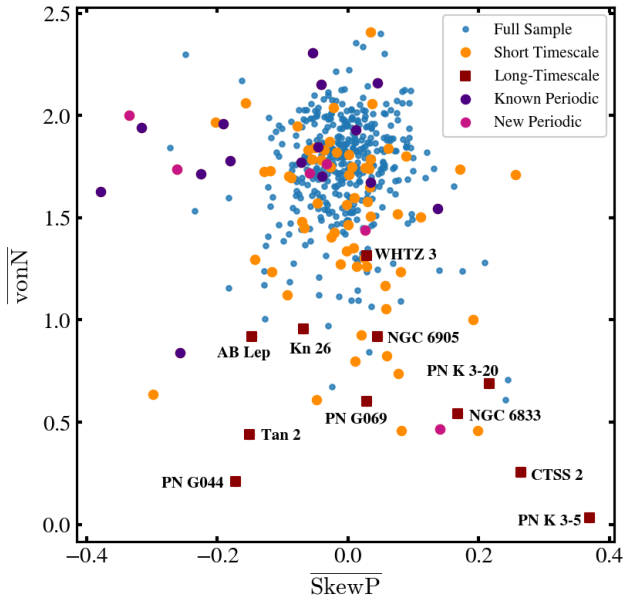

Figure A1. The position of the ZTF-variable CSPNe in the two-dimensional variability metric space defined by the Von-Neumann statistics (vonN) and Pearson-Skew (SkewP) metrics (see Equations (B1) and (B2) in Paper I). This is the same as Figure 8 in Paper I, with the long-timescale variables labeled individually. All of them are characterized by a low value of Vonn ($<$1), making them easily identifiable. The value of SkewP provides further information on the nature of the variability (brightening/outburst vs. dimming/transits).

in these sources is well resolved in ZTF cadence and, thus, non-random. Based on the light curves presented in the main paper, the values of SkewP are easy to interpret. Sources showing brightening events, like NGC 6833, CTSS 2, K 3-5, and K 3-20, have SkewP > 0. Whereas objects showing dips like AB Lep or Tan 2 have SkewP < 0. The variability in NGC 6905 and Kn 26 is symmetric, thus they don't have significant positive or negative SkewP values. The SkewP values of the more complex variables like PN G044.3+04.1 can be difficult to interpret. Nevertheless, most of the long-timescale variables stand out from the other objects in the space and are easily identifiable. This thus potentially serves as a great tool to filter interesting sources from large data sets of light curves.

Appendix B
Optical Spectrum of NGC 6833

NGC 6833 was observed with the DouBle SPectrograph (DBSP; Oke & Gunn 1982) attached to the Cassegrain focus of the Palomar 200 in Hale Telescope. We used the D55 dichroic, the 600 line mm^{-1} grating for the blue arm blazed at 3780 Å, and the 316 line mm^{-1} grating for the red arm blazed at 7150 Å. We used grating angles of 27°17′ and 24°38′ for the blue and red sides, respectively. With these setups and a slit width of 1.″5 long-slit, we achieve resolving powers of $R = 1600$ in the blue arm and $R = 1400$ in the red arm. These setups provide continuous spectral coverage across 2900–10800 Å, with the division between blue and red arms typically occurring around 5650 Å. We followed the same reduction procedure as described in Section 4.2.1 in Paper I. Briefly, we used PypeIt (Prochaska et al. 2020a, 2020b) with the options `use_2dmodel_mask = False` and `no_local_sky = True` to avoid masking and local subtraction of the strong emission lines. Following this, we perform manual trace identification on the two-dimensional spectrum.

Figure B1 shows the optical spectrum for NGC 6833. Given the very compact nature of the nebula, the spectrum is completely dominated by the nebular continuum and the emission lines. No stellar signature can be observed in the current spectrum.

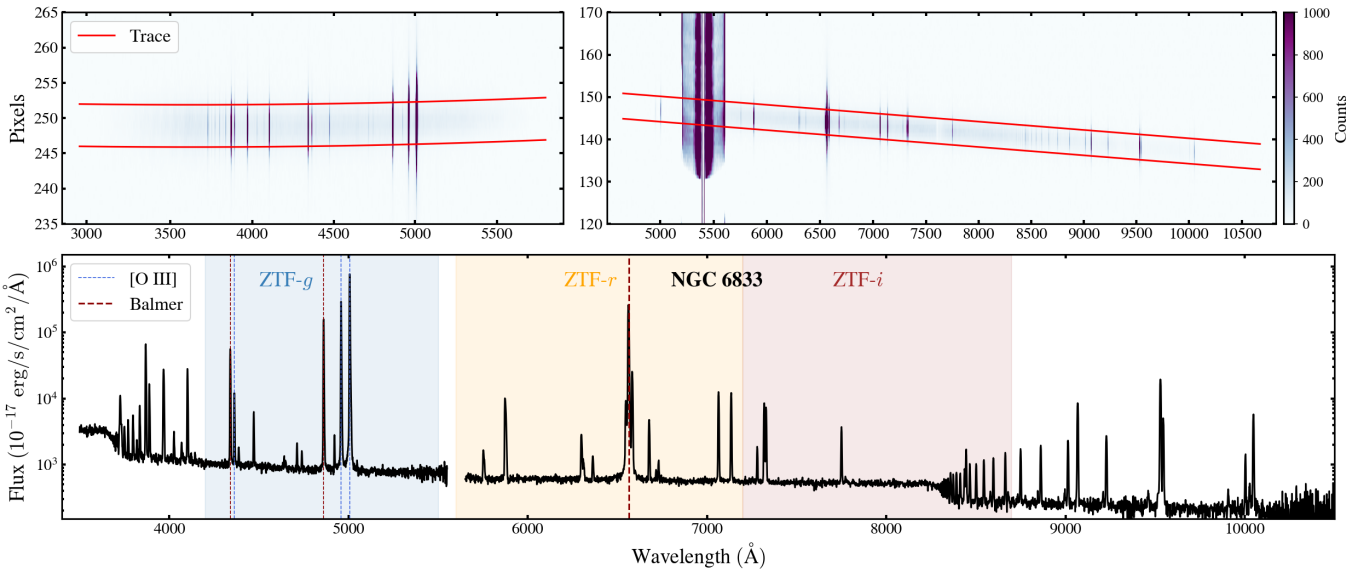

Figure B1. The DBSP spectrum for NGC 6833. The upper left and right panels show the two-dimensional spectra for the blue and the red arms respectively. The bottom panel shows the one-dimensional spectrum derived from the marked trace. We mark the first three Balmer and [O III] emission lines in the spectrum. We also shade the approximate ZTF band passes.

Appendix C
Optical Spectrum of Kn 26

We took four 900 s exposures of Kn 26 at the twin 8.4 m Large Binocular Telescope (LBT) using the Multi-Object Double Spectrographs (MODS, Pogge et al. 2010) on 2024 December. MODS provides two-channel grating spectroscopy by using a dichroic that splits the light at ≈5650 Å into separately optimized red and blue channels. The spectra cover the wavelength region 3330–5800 Å and 5500–10000 Å with a resolving power of $R \approx 1850$ and 2300, respectively. The spectra were reduced using the modsccdred[27] PYTHON package (Pogge 2019) for basic 2d CCD reductions, and the modsidl[28] pipeline (Croxall & Pogge 2019) to extract 1 day spectra and apply wavelength and flux calibrations.

The coadded MODS spectrum is shown in Figure C1. We note that the Balmer and He II lines appear to be a super composition of a narrow emission line (likely resulting from the PN) and weaker but broader emission line (possibly originating from the photosphere). We identify the N III C III C IV emission line complex around 4650 Å but note that the the C IV 5801, 5812 Å doublet is not visible. Therefore, Kn 26 can be considered as a weak emission-line type ([WELS]) central star (Marcolino & de Araújo 2003). We note here that the emission lines can also arise from the irradiated companion (as often the case with WELS type PN nuclei, see for example Miszalski et al. 2011a), and can be an indirect confirmation of the binarity of the system.

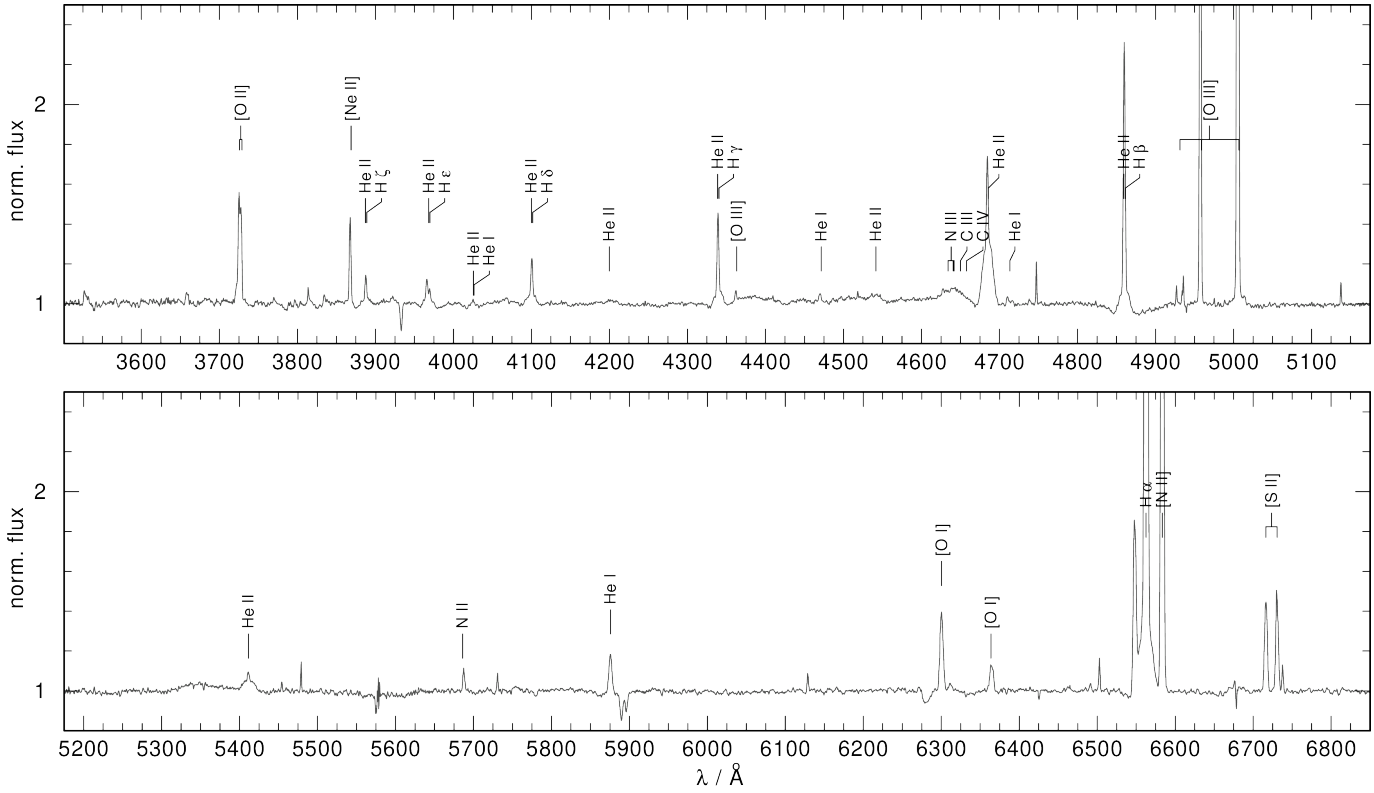

Figure C1. LBT/MODS spectrum of the WELS type central star of Kn 26.

[27] https://github.com/rwpogge/modsCCDRed
[28] https://github.com/rwpogge/modsIDL

Appendix D
NGC 6905 and Kn 26 Periodicity Tests

We briefly describe here the various tests performed to confirm the reality of the inferred periods of NGC 6905 and Kn 26. Though not shown, the periods were recovered from standard photometry data too, ruling out any difference image artifact. To check if the observed variability is due to seasonal variation in atmospheric conditions, we compared the atmospheric seeing to the observed flux. No correlation was found. To test if the periods arise from the seasonal breaks or yearly cycles in the survey, we randomized the flux values keeping the time stamps constant, and manually investigated the periodogram in several iterations. No significant peak was obtained and the periodograms were as good as noise. This is also reflected as a negligible false alarm probability (FAP) calculated using the inbuilt bootstrap method in `astropy.timeseries`.

We then query ZTF standard photometry light curves of all Gaia sources within a couple of arcminutes from the targets (∼200 objects for each source). Visually, none of the neighboring objects showed the variability seen in the target sources. These include sources behind the extended nebulae of the PNe, thus ruling out any spurious nebular activity resulting in the observed modulation. We applied the same period search procedure on all neighboring objects' light curves and manually inspected the periodograms. For the most significant period in each of the resultant periodograms, we investigate the distribution of the FAPs. None of the objects showed the periods inferred in our targets with any reasonable FAP or periodogram signal to noise. The only two spurious periods with low FAP in some of the objects are one year and ∼2000 days (the ZTF baseline), but nowhere close to the inferred periods in the two targets.

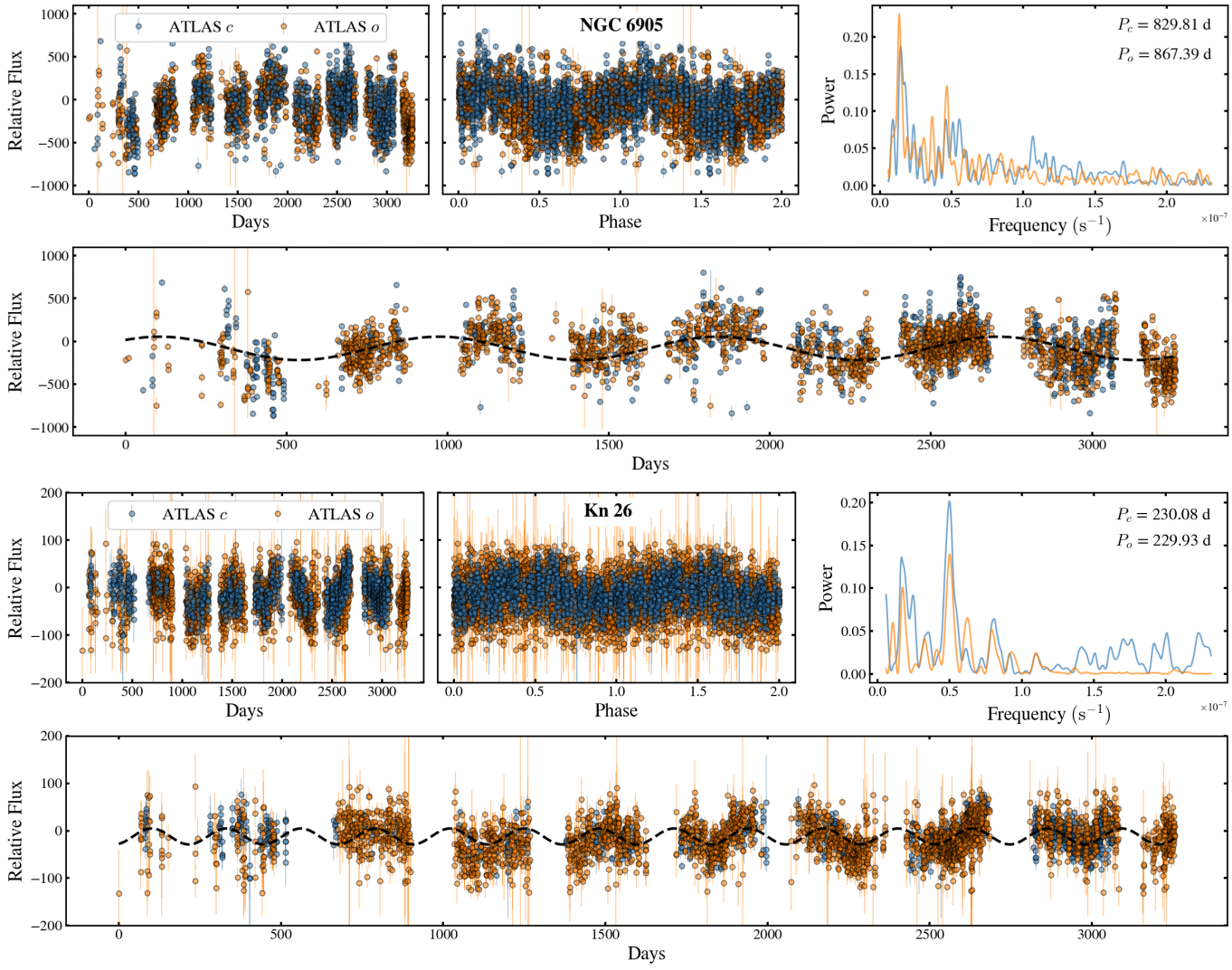

Figure D1. Same as Figure 3, but with ATLAS light curve, for both NGC 6905 (upper section) and Kn 26 (lower section). Similar periods (same for Kn 26) as in ZTF are recovered, ruling out any ZTF-specific systematics.

For a final test, we queried the difference-image forced photometry data from the Asteroid Terrestrial-impact Last Alarm System (ATLAS) survey[29] for both the targets and perform period search. The results are presented in Figure D1. Qualitatively, similar variability as in ZTF is recovered in ATLAS. This rules out with confidence both any ZTF-specific systematics and region-specific atmospheric seeing variation inducing the variability. Significant peak in the periodogram appears for NGC 6905, albeit at a slightly higher period of ∼850 days. The disagreement may result from the ATLAS data being significantly noisier than ZTF. A secondary peak at a similar period as in ZTF is recovered. For Kn 26, we successfully recovered the dominant ZTF period of ∼230 days. The secondary peak in ATLAS has a lower signal-to-noise, but the corresponding period is broadly in agreement with that in ZTF. We briefly note here that ATLAS data is too noisy to detect the short period in Kn 26.

Appendix E
DBSP Spectra of CTSS 2 and K 3-5

Figure E1 shows the DBSP spectrum for CTSS 2 and K 3-5. The same reduction was procedure as with WeSb 1 in Paper I and NGC 6833 was followed. With a slit spectrograph, it is difficult to separately identify the nucleus and the nebula. Thus, we choose a fiducial trace containing the main emission core and extract the corresponding one-dimensional spectra. The only advantage over the previously presented HET spectrum is its better spectral coverage in the red. This enables us to check for obvious indication of a giant star, which may indicate a symbiotic system. Such signatures are not present in the spectrum.

[29] We queried both the difference and science-image forced photometry data from the online service at https://fallingstar-data.com/forcedphot/ (Shingles et al. 2021). Owing to their warnings about the latter, we primarily use the former but use the science-image data for estimation of the reference flux and normalization. We reject all data where `err` ≠ 0.

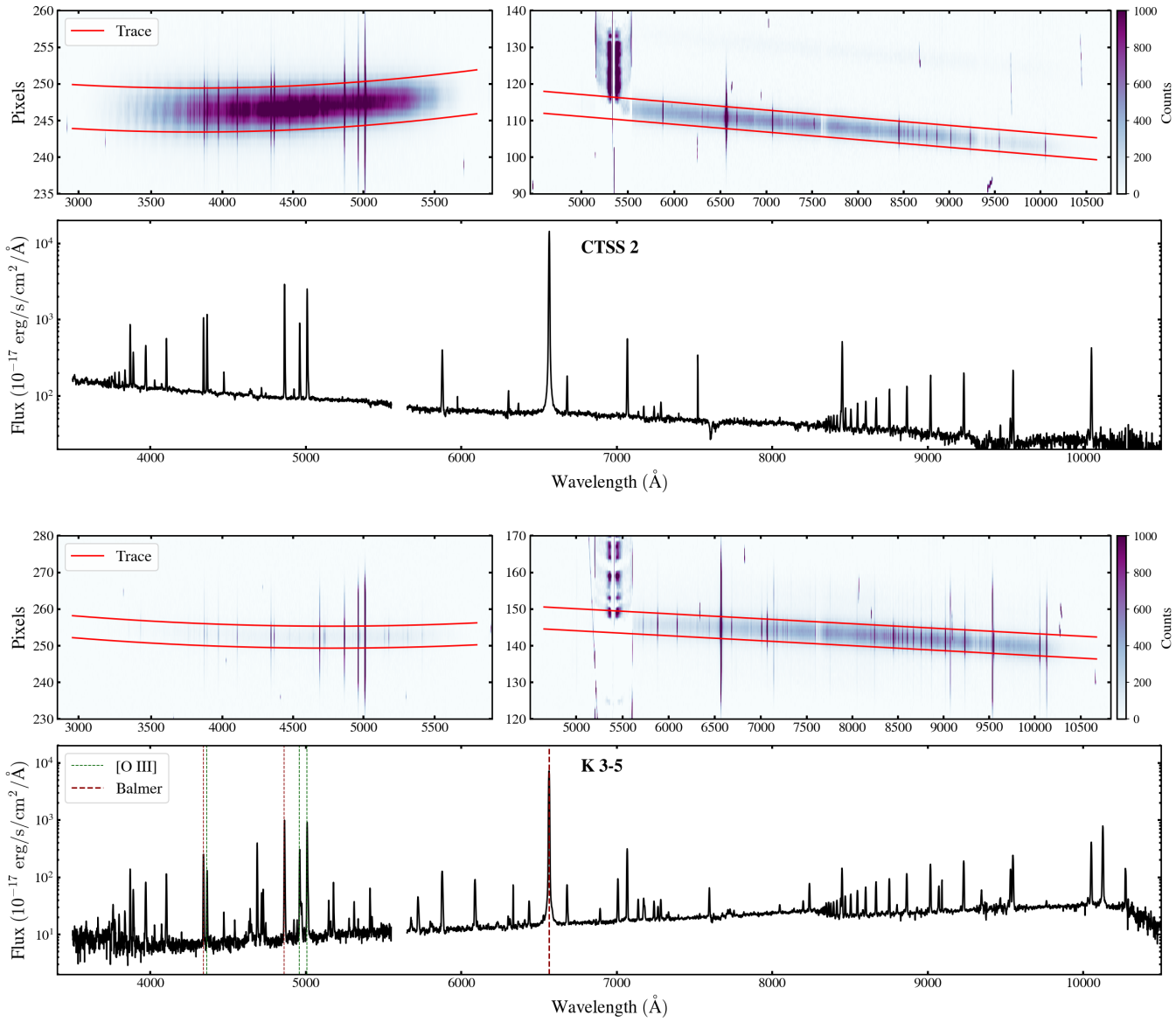

Figure E1. DBSP spectra of CTSS 2 (upper section) and K 3-5 (lower section) in the same format as Figure B1.

Appendix F
Infrared Excess in CTSS 2 and K 3-5

Long term dust production is a possible explanation to the reddened brightening of CTSS 2 and K 3-5. Thus, to look for the presence of dust in these systems, we investigate their spectral energy distributions (SED). The result is presented in Figure F1. Some scatter is evident in the data, especially for K 3-5, which is possibly due to the extended nature of the objects leading to suboptimal photometry. Nevertheless, the presence of significant infrared excess in both the objects is evident.

For a more quantitative estimate, we perform multi-component blackbody fit to the data points with wavelengths $>1\,\mu$m. For CTSS 2, a reasonable fit was obtained with a two-component fit. The stellar component was subtracted and distance of 8 kpc was assumed. For K 3-5, we assumed the Gaia eDR3 parallax distance of 2481 pc, and a reasonable fit was only observed with three components. The fit parameters of the different components are presented are annotations in the same Figure F1.

We interpret the various blackbody components as representative of extended dust structures. We find that both CTSS 2 and K 3-5 appear to have warm dust with temperature in the range of T =1000–1500 K and radius R =50–100 $R_\odot$. We also find evidence of extended colder dust features. For K 3-5 it appears to be extended to around a thousand

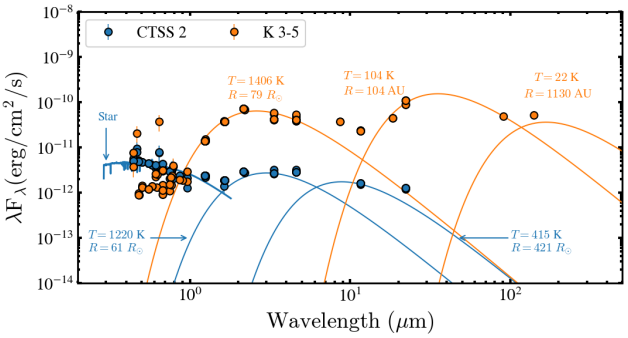

Figure F1. Spectral energy distribution (SED) of CTSS 2 (blue) and K 3-5 (orange). Significant infrared excess is evident. The blackbody fits the long-wavelength (>1 μm) data are shown along with the inferred parameters. We interpret them as warm and cold dust structures. The Vizier query also yields fluxes at radio wavelengths (1.4 GHz and 5 GHz). They likely do not relate to our analysis (as the radio emissions are often of non-thermal origin) and thus we have disregarded them.

astronomical unit, with $T \lesssim 100$ K. For CTSS 2, the second component appears hotter and more localized to around $400\,R_\odot$. But this might be due to inadequate coverage in the redder wavelengths, thus missing out on the more extended cooler dust components.

ORCID iDs

Soumyadeep Bhattacharjee https://orcid.org/0000-0003-2071-2956
Nicole Reindl https://orcid.org/0000-0002-0119-7883
Howard E. Bond https://orcid.org/0000-0003-1377-7145
Klaus Werner https://orcid.org/0000-0002-6428-2276
Gregory R. Zeimann https://orcid.org/0000-0003-2307-0629
David Jones https://orcid.org/0000-0003-3947-5946
Kareem El-Badry https://orcid.org/0000-0002-6871-1752
Nina Mackensen https://orcid.org/0009-0006-3864-7645
Nicholas Chornay https://orcid.org/0000-0002-8767-3907
S. R. Kulkarni https://orcid.org/0000-0001-5390-8563
Ilaria Caiazzo https://orcid.org/0000-0002-4770-5388
Jan van Roestel https://orcid.org/0000-0002-2626-2872
Antonio C. Rodriguez https://orcid.org/0000-0003-4189-9668
Thomas A. Prince https://orcid.org/0000-0002-8850-3627
Ben Rusholme https://orcid.org/0000-0001-7648-4142
Russ R. Laher https://orcid.org/0000-0003-2451-5482
Roger Smith https://orcid.org/0000-0001-7062-9726

References

Aller, A., Lillo-Box, J., & Jones, D. 2024, A&A, 690, A190
Aller, A., Lillo-Box, J., Jones, D., Miranda, L. F., & Barceló Forteza, S. 2020, A&A, 635, A128
Aller, L. H., & Liller, W. 1966, MNRAS, 132, 337
Arkhipova, V. P., Burlak, M. A., Esipov, V. F., Ikonnikova, N. P., & Komissarova, G. V. 2012, AstL, 38, 157
Arkhipova, V. P., Burlak, M. A., Esipov, V. F., Ikonnikova, N. P., & Komissarova, G. V. 2013, AstL, 39, 619
Arkhipova, V. P., Burlak, M. A., Ikonnikova, N. P., et al. 2020, AstL, 46, 100
Asplund, M., Gustafsson, B., Lambert, D. L., & Kameswara Rao, N. 1997, A&A, 321, L17
Astropy Collaboration, Price-Whelan, A. M., Sipőcz, B. M., et al. 2018, AJ, 156, 123
Astropy Collaboration, Robitaille, T. P., Tollerud, E. J., et al. 2013, A&A, 558, A33
Bailer-Jones, C. A. L., Rybizki, J., Fouesneau, M., Demleitner, M., & Andrae, R. 2021, AJ, 161, 147
Balick, B., & Frank, A. 2002, ARA&A, 40, 439
Bhattacharjee, S., Kulkarni, S. R., Kong, A. K. H., et al. 2025, PASP, 137, 024201
Boffin, H. M. J., & Jones, D. 2019, The Importance of Binaries in the Formation and Evolution of Planetary Nebulae (Switzerland AG: Springer)
Bollen, D., Van Winckel, H., & Kamath, D. 2017, A&A, 607, A60
Bond, H. E., Chaturvedi, A. S., Ciardullo, R., et al. 2024, ApJ, 970, 164
Bond, H. E., & Livio, M. 1990, ApJ, 355, 568
Bond, H. E., & Meakes, M. G. 1990, AJ, 100, 788
Bond, H. E., Werner, K., Jacoby, G. H., & Zeimann, G. R. 2023, MNRAS, 521, 668
Bond, H. E., & Zeimann, G. R. 2024, ApJ, 967, 122
Budaj, J., Bernhard, K., Jones, D., & Munday, J. 2025, NatAs, 9, 380
Chen, P., Fang, X., Chen, X., & Liu, J. 2025, ApJ, 980, 227
Chen, Z., Frank, A., Blackman, E. G., Nordhaus, J., & Carroll-Nellenback, J. 2017, MNRAS, 468, 4465
Choi, J., Dotter, A., Conroy, C., et al. 2016, ApJ, 823, 102
Chonis, T. S., Hill, G. J., Lee, H., Tuttle, S. E., & Vattiat, B. L. 2014, Proc. SPIE, 9147, 91470A
Chonis, T. S., Hill, G. J., Lee, H., et al. 2016, Proc. SPIE, 9908, 99084C
Chornay, N., & Walton, N. A. 2021, A&A, 656, A110
Ciardullo, R., & Bond, H. E. 1996, AJ, 111, 2332
Clayton, G. C., & De Marco, O. 1997, AJ, 114, 2679
Córsico, A. H., Uzundag, M., Kepler, S. O., et al. 2021, A&A, 645, A117
Croxall, K. V., & Pogge, R. W. 2019, rwpogge/modsIDL: modsIDL Binocular Release, v1.0, Zenodo, doi:10.5281/zenodo.2561424
Culpan, R., Geier, S., Reindl, N., et al. 2022, A&A, 662, A40
Decleir, M., Gordon, K. D., Andrews, J. E., et al. 2022, ApJ, 930, 15
De Marco, O. 2009, PASP, 121, 316
Dotter, A. 2016, ApJS, 222, 8
El-Badry, K., Rix, H.-W., Tian, H., Duchêne, G., & Moe, M. 2019, MNRAS, 489, 5822
Faltová, N., Kallová, K., Prišegen, M., et al. 2021, A&A, 656, A125
Feline, W. J., Dhillon, V. S., Marsh, T. R., Watson, C. A., & Littlefair, S. P. 2005, MNRAS, 364, 1158
Fitzpatrick, E. L., Massa, D., Gordon, K. D., Bohlin, R., & Clayton, G. C. 2019, ApJ, 886, 108
Froebrich, D., Hillenbrand, L. A., Herbert, C., et al. 2023, MNRAS, 520, 5413
García-Hernández, D. A., & Górny, S. K. 2014, A&A, 567, A12
Gezer, I., Van Winckel, H., Bozkurt, Z., et al. 2015, MNRAS, 453, 133
Ginsburg, A., Sipőcz, B. M., Brasseur, C. E., et al. 2019, AJ, 157, 98
Gómez-González, V. M. A., Rubio, G., Toalá, J. A., et al. 2022, MNRAS, 509, 974
Gómez-Muñoz, M. A., Bianchi, L., & Manchado, A. 2023, ApJS, 266, 34
Gonzalez, G., Lambert, D. L., Wallerstein, G., et al. 1998, ApJS, 114, 133
Gordon, K. 2024a, dust_extinction: Interstellar Dust Extinction Models, v1.5, Zenodo, doi:10.5281/zenodo.4658887
Gordon, K. 2024b, JOSS, 9, 7023
Gordon, K. D., Cartledge, S., & Clayton, G. C. 2009, ApJ, 705, 1320
Gordon, K. D., Clayton, G. C., Decleir, M., et al. 2023, ApJ, 950, 86
Gordon, K. D., Misselt, K. A., Bouwman, J., et al. 2021, ApJ, 916, 33
Graham, M. J., Kulkarni, S. R., Bellm, E. C., et al. 2019, PASP, 131, 078001
Gröbel, R., Hümmerich, S., Paunzen, E., & Bernhard, K. 2017, NewA, 50, 104
Guerrero, M. A., Miranda, L. F., Ramos-Larios, G., & Vázquez, R. 2013, A&A, 551, A53
Hajduk, M., van Hoof, P. A. M., Gesicki, K., et al. 2014, A&A, 567, A15
Hajduk, M., Zijlstra, A. A., & Gesicki, K. 2008, A&A, 490, L7
Handler, G., Mendez, R. H., Medupe, R., et al. 1997, A&A, 320, 125
Harris, C. R., Millman, K. J., van der Walt, S. J., et al. 2020, Natur, 585, 357
Hart, K., Shappee, B. J., Hey, D., et al. 2023, arXiv:2304.03791
Heber, U., Irrgang, A., & Schaffenroth, J. 2018, OAst, 27, 35
Hill, G. J., Lee, H., MacQueen, P. J., et al. 2021, AJ, 162, 298

Hunter, J. D. 2007, CSE, 9, 90
Husser, T. O., Wende-von Berg, S., Dreizler, S., et al. 2013, A&A, 553, A6
Hyung, S., Lee, S.-J., & Kim, M.-H. 2010, JKPS, 57, 514
Irrgang, A., Geier, S., Heber, U., et al. 2021, A&A, 650, A102
Ivezić, Ž., Kahn, S. M., Tyson, J. A., et al. 2019, ApJ, 873, 111
Jacob, R., Schönberner, D., & Steffen, M. 2013, A&A, 558, A78
Jacoby, G. H., Hillwig, T. C., Jones, D., et al. 2021, MNRAS, 506, 5223
Jeffery, C. S., & Hambsch, F. J. 2019, MNRAS, 487, 4128
Jeffery, C. S., & Schönberner, D. 2006, A&A, 459, 885
Jones, D., & Boffin, H. M. J. 2017, NatAs, 1, 0117
Jones, D., Van Winckel, H., Aller, A., Exter, K., & De Marco, O. 2017, A&A, 600, L9
Kővári, Z., Strassmeier, K. G., Oláh, K., et al. 2019, A&A, 624, A83
Kiss, L. L., & Bódi, A. 2017, A&A, 608, A99
Kiss, L. L., Szabó, G. M., & Bedding, T. R. 2006, MNRAS, 372, 1721
Kostyakova, E. B., & Arkhipova, V. P. 2009, ARep, 53, 1155
Lawlor, T. M. 2023, MNRAS, 519, 5373
Lee, H.-W., Kang, Y.-W., & Byun, Y.-I. 2001, ApJL, 551, L121
Liebert, J., Bond, H. E., Dufour, P., et al. 2013, ApJ, 769, 32
Lomb, N. R. 1976, Ap&SS, 39, 447
Manick, R., Miszalski, B., Kamath, D., et al. 2021, MNRAS, 508, 2226
Marcolino, W. L. F., & de Araújo, F. X. 2003, AJ, 126, 887
Martínez, C. I., Mauas, P. J. D., & Buccino, A. P. 2022, MNRAS, 512, 4835
Masci, F. J., Laher, R. R., Rusholme, B., et al. 2019, PASP, 131, 018003
Miller Bertolami, M. M. 2016, A&A, 588, A25
Miszalski, B., Acker, A., Moffat, A. F. J., Parker, Q. A., & Udalski, A. 2009a, A&A, 496, 813
Miszalski, B., Acker, A., Parker, Q. A., & Moffat, A. F. J. 2009b, A&A, 505, 249
Miszalski, B., Corradi, R. L. M., Boffin, H. M. J., et al. 2011a, MNRAS, 413, 1264
Miszalski, B., Mikołajewska, J., Köppen, J., et al. 2011b, A&A, 528, A39
Moreno-Ibáñez, M., Villaver, E., Shaw, R. A., & Stanghellini, L. 2016, A&A, 593, A29
Muzerolle, J., Furlan, E., Flaherty, K., Balog, Z., & Gutermuth, R. 2013, Natur, 493, 378
Nicholls, C. P., Wood, P. R., Cioni, M. R. L., & Soszyński, I. 2009, MNRAS, 399, 2063
Oke, J. B., & Gunn, J. E. 1982, PASP, 94, 586
Oliveira da Rosa, G., Kepler, S. O., Soethe, L. T. T., Romero, A. D., & Bell, K. J. 2024, ApJ, 974, 314
Osterbrock, D. E., & Ferland, G. J. 2006, Astrophysics of Gaseous Nebulae and Active Galactic Nuclei (2nd; Sausalito, CA: Univ. Science Books)
pandas development team T. 2020, pandas-dev/pandas: Pandas, latest v2.3.2, Zenodo, doi:10.5281/zenodo.3509134
Parker, Q. A., Bojičić, I. S., & Frew, D. J. 2016, JPhCS, 728, 032008
Pawlak, M. 2021, A&A, 649, A110
Paxton, B., Bildsten, L., Dotter, A., et al. 2011, ApJS, 192, 3
Paxton, B., Cantiello, M., Arras, P., et al. 2013, ApJS, 208, 4
Paxton, B., Marchant, P., Schwab, J., et al. 2015, ApJS, 220, 15
Pereyra, M., Richer, M. G., & López, J. A. 2013, ApJ, 771, 114
Pogge, R. 2019, rwpogge/modsCCDRed: v2.0.1, Zenodo, doi:10.5281/zenodo.2647501
Pogge, R. W., Atwood, B., Brewer, D. F., et al. 2010, Proc. SPIE, 7735, 77350A
Prochaska, J., Hennawi, J., Cooke, R., et al. 2020a, pypeit/PypeIt: Release, v1.0.0, Zenodo, doi:10.5281/zenodo.3743493
Prochaska, J., Hennawi, J., Westfall, K., et al. 2020b, JOSS, 5, 2308
Ramsey, L. W., Adams, M. T., Barnes, T. G., et al. 1998, Proc. SPIE, 3352, 34
Reindl, N., Islami, R., Werner, K., et al. 2023, A&A, 677, A29
Reindl, N., Rauch, T., Miller Bertolami, M. M., Todt, H., & Werner, K. 2017, MNRAS, 464, L51
Reindl, N., Rauch, T., Parthasarathy, M., et al. 2014, A&A, 565, A40
Rosenbush, A. É., & Efimov, Y. S. 2015, Ap, 58, 46
Scargle, J. D. 1982, ApJ, 263, 835
Schaefer, B. E., & Edwards, Z. I. 2015, ApJ, 812, 133
Shappee, B. J., Prieto, J. L., Grupe, D., et al. 2014, ApJ, 788, 48
Shingles, L., Smith, K. W., Young, D. R., et al. 2021, TNSAN, 7, 1
Soszyński, I., Olechowska, A., Ratajczak, M., et al. 2021, ApJL, 911, L22
Stanghellini, L., Shaw, R. A., & Villaver, E. 2016, ApJ, 830, 33
Tyndall, A. A., Jones, D., Boffin, H. M. J., et al. 2013, MNRAS, 436, 2082
van Genderen, A. M., & Gautschy, A. 1995, A&A, 294, 453
Van Winckel, H., Jorissen, A., Exter, K., et al. 2014, A&A, 563, L10
Van Winckel, H., Waelkens, C., Fernie, J. D., & Waters, L. B. F. M. 1999, A&A, 343, 202
VanderPlas, J. T. 2018, ApJS, 236, 16
Virtanen, P., Gommers, R., Oliphant, T. E., et al. 2020, NatMe, 17, 261
von Neumann, J. 1941, The Annals of Mathematical Statistics, 12, 367
Weidmann, W., Gamen, R., Mast, D., et al. 2018, A&A, 614, A135
Werner, K., Deetjen, J. L., Dreizler, S., et al. 2003, in ASP Conf. Ser. 288, Stellar Atmosphere Modeling, ed. I. Hubeny, D. Mihalas, & K. Werner (San Francisco, CA: ASP), 31
Werner, K., Rauch, T., & Reindl, N. 2019, MNRAS, 483, 5291
Werner, K., Reindl, N., Löbling, L., et al. 2020, A&A, 642, A228
Wright, S. A., Corradi, R. L. M., & Perinotto, M. 2005, A&A, 436, 967